# Editorial letter:

On the Aims & Scopes of ***Radiation Physics and Engineering***

Radiation Physics and Engineering (RPE) is an international scientific-research journal published biannual by K. N. Toosi University of Technology jointly with Nuclear Society of Iran (NSI).

The purposes of the journal are to provide a high quality medium for the publication of substantial, original and scientific papers on the development and the enhancement of radiation physics and radiation engineering researches at the national as well as international level. In addition, we hope to facilitate communication among physicists, to publish the results of research, develop collaboration between research workers from different research centers and universities and introduce young researchers.

Papers dealing with nuclear radiation and radionuclide techniques, nuclear techniques and radiation processing, nuclear energy science and technology and nuclear physics in both experimental and theoretical fields, applied in physics, chemistry, biophysics, biology, medicine, medical physics, engineering and environmental sciences are welcome.

Relevant topics for RPE include the following:

- Nuclear Reactor Technology: design, calculations, measurements.
- Radiation Sources: design, construction, production, characteristics, activation cross-sections, target design, processing, quality control procedures.
- Particle Accelerators Ion Sources: beam transport systems and target arrangements as well as the use of secondary phenomena such as synchrotron radiation and free electron lasers: design, applications, calculations and measurements.
- Fusion: related technology and equipment, measurements and calculations.
- Measurement of Radiation and Radioactivity: measurement of X-rays, $\gamma$-rays, $\alpha$- and $\beta$-particles and other forms of radiation; nuclear instrumentation, including radiation spectrometry, dosimetry, novel counting systems and whole-body counters, novel radiation detector systems.
- Radioanalytical Methods and Radiochemistry: activation analysis, isotope dilution analysis, radioimmunoassay, radionuclide tomography, radiation spectrometry, synthesis of labelled compounds, chemical behavior and speciation of radionuclides.
- Nuclear Physics: nuclear structure, nucleon-nucleon interaction, nuclear reactions, Hadronic physics, few-body problems, effective filed theory.

Types of article:

- Full-length article: unlimited number of pages and figures, following the Full-length articles, which should be definitive and describe a reasonably complete investigation.
- Review article: submitted only by request and with previous agreement of the Editors.
- Technical note: specifically addressing technical issues not qualifying as original research work.
- Discussion: questioning the content of published articles by other authors.

## GUIDELINES AND POLICIES

**Ethical Responsibilities of Authors**

Authors should observe the following codes of conduct when they intend to submit/publish a paper. Maintaining integrity of the research and its presentation can be achieved by following the rules of good scientific practice, which include:

- The manuscript has not been submitted to more than one journal for simultaneous consideration.
- The manuscript has not been published previously (partly or in full), unless the new work concerns an expansion of previous work (please provide transparency on the re-use of material to avoid the hint of text-recycling (self-plagiarism)).
- A single study is not split up into several parts to increase the quantity of submissions and submitted to various journals or to one journal over time.
- No data have been fabricated or manipulated (including images) to support your conclusions.
- No data, text, or theories by others are presented as if they were the authors own (plagiarism). Proper acknowledgements to other works must be given (this includes material that is closely copied (near verbatim), summarized and/or paraphrased), quotation marks are used for verbatim copying of material, and permissions are secured for material that is copyrighted.
- Important note: the journal may use software to screen for plagiarism. The plagiarism is checked through two methods: reviewer check and plagiarism prevention tool (iThenticate). All submissions will be checked by online software before being sent to reviewers.
- Consent to submit has been received explicitly from all co-authors, as well as from the responsible authorities - tacitly or explicitly - at the institute/organization where the work has been carried out, before the work is submitted.
- Authors whose names appear on the submission have contributed sufficiently to the scientific work and therefore share collective responsibility and accountability for the results.
- Changes of authorship or in the order of authors are not accepted after acceptance of a manuscript. Authors are expected to consider carefully the list and order of authors before submitting their manuscript and provide the definitive list of authors at the time of the original submission. Any addition, deletion or rearrangement of author names in the authorship list should be made only before the manuscript has been accepted and only if approved by the journal Editor. To request such a change, the Editor must receive the following from the corresponding author: (a) the reason for the change in author list and (b) written confirmation (e-mail, letter) from all authors that they agree with the addition, removal or rearrangement. In the case of addition or removal of authors, this includes confirmation from the author being added or removed.

For more information about instructions to authors and preparing a manuscript for submission, please visit journal website: **http://rpe.kntu.ac.ir**

# Radiation Physics and Engineering

**ISSN 2645-6397**

**An international scientific-research journal published quarterly by K.N. Toosi University of Technology jointly with Nuclear Society of Iran**

**Vol. 3, Issue 4, Autumn 2022**

# Contents

RPE | Radiation Physics & Engineering
An International Peer-Reviewed Journal
Published by K.N. Toosi University of Technology
http://rpe.kntu.ac.ir
Research Article

Radiation Physics and Engineering 2022; 3(4):1–5
https://doi.org/10.22034/rpe.2022.336199.1069

# Design and simulation of an S-Band tunable solid-state power amplifier as an RF injector into a miniature ECR ion source

Hamid Rahimpour*, HamidReza Mirzaei, Masoomeh Yarmohammadi Satri, Zafar Riazi Mobaraki
*Physics and Accelerators Research School, NSTRI, P.O. Box 14395-836, Tehran, Iran*

## HIGHLIGHTS

- A high-power RF MOSFET transistor is utilized to design a solid-state power source.
- The RF transistor is internally matched to 50 ohms and doesnt need any bias sequence circuit.
- The proposed RF source can deliver 57 dBm of power into the ECR ion source.

## ABSTRACT

A continuous-wave solid-state-based power amplifier is designed and simulated in this paper to work as an RF injector into an ECR ion source chamber. Employing a solid-state radio frequency power amplifier, instead of microwave tubes, leads to having higher efficiency, lower price, compact size, and longer lifetime. Also, a modular design can be achieved for designing higher output power by repeating lower power sources and combining them. The proposed solid-state source can deliver more than 200 W power to the ion chamber with a single high-power transistor. The selected Doherty high-power transistor is internally matched to 50 ohms and does not need a bias sequence circuit. Two gain stages are applied to drive the high-power transistor. The designed RF source is simulated using the Advanced Design System (ADS) based on the measured scattering parameters of components. Simulations show an output power of more than 57 dBm with a tunable frequency bandwidth from 2.3 to 2.5 GHz.

## KEYWORDS

Power amplifier
Solid-state transistors
Power efficiency
RF source
Ion source

## HISTORY

Received: 6 April 2022
Revised: 30 May 2022
Accepted: 10 June 2022
Published: Autumn 2022

## 1 Introduction

Transistor-based power amplifiers are much more efficient than microwave tubes like magnetrons and have a longer lifetime, higher efficiency, and more compatibility to be designed with other electronic components (Piel et al., 2005). It significantly improves the minimization of size, cost and can have better control over power management and impedance matching (Nakatani and Ishizaki, 2015). As a result, these features give them the ability to be utilized in miniature Electron Cyclotron Resonance (ECR) ion sources (Fatkullin et al., 2018; Wen et al., 2018).

The main solid-state-based design considerations are the number of high-power transistors for reaching the desired output power, bias sequence control, frequency stability, efficiency, and matching networks (Bondarenko et al., 2019; Latrasse et al., 2017; Piel et al., 2005; Tuo et al., 2009). Usually, microstrip-based matching networks are used for delivering the maximum output power. Also, the number of high-power transistors is important because several power combiners should be used which can dissipate power before reaching load (Chen et al., 2017; Duc et al., 2018).

In the present work, we hired an internally matched transistor, on both the output and input sides which can deliver up to 57 dBm power at S-band frequencies. In our previous work, we proposed a power chain in which the main power transistor needed negative gate voltage. Rf transistors with negative gate voltage need bias power-up and power-down sequence control. As the selected high-power transistor in this paper works with positive gate voltage, it does not need any bias sequence circuit and additional matching networks. As a result, the design procedure becomes simple and more reliable. Using an internally matched transistor with high efficiency which requires a positive gate voltage is the main novelty of our structure. The dimension of the target plasma chamber is considered $50 \times 50$ mm$^2$. It utilizes an alumina window

*Corresponding author: hrahimpour@aeoi.org.ir

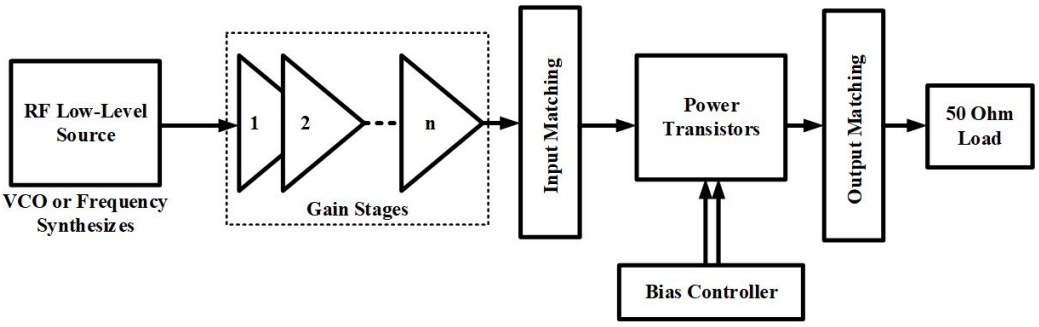


**Figure 1:** Basic block diagram of a solid-state based RF source.

as a lens for microwave power coupling to focus the wave into the chamber.

This article is organized as follows: Section 2 describes different types of high power sources. The proposed solid-state source is expressed in detail in Section 3. Results are shown in Section 4 and finally, the paper ends with a conclusion and references.

## 2 Types of high-power sourc

There are different types of high-power RF sources that can be categorized into two main parts; microwave tubes and solid-state power amplifiers. Travelling Wave Tubes (TWT), klystron tubes, and magnetrons are different types of microwave tubes. Microwave tubes are usually utilized to reach an output power in the range of mega wats while solid-state power amplifiers can be applied for lower power ranges. Output power, frequency bandwidth, power efficiency, frequency stability, and lifetime are usually the main parameters of an RF source. Usually, solid-state amplifiers have a higher power efficiency, longer lifetime, lower cast, and smaller size in comparison with microwave tubes. Also, magnetrons and klystrons need a high voltage while solid-state amplifiers work with much lower voltages. Indeed, solid-state amplifiers in ion source accelerator applications are a good choice for delivering medium power ranges of about several kilowatts. As the target load in this article is a compact electron cyclotron resonance ion source and can be triggered by at least 200 W to 1 kW, the best choice is a solid-state power source.

Figure 1 shows a basic block diagram of a solid-state RF source. It usually needs a local oscillator or frequency synthesizer as a low-level RF source. This power at the specific frequency will be amplified with several gain stages to drive the main power transistors. Input and output matching networks can be utilized to maximize the output power. There are two types of high-power metal-oxide-semiconductor field-effect transistor (MOSFET); enhanced mode and depletion mode. In enhanced mode MOSFET transistors, a positive voltage should be applied to the gate while in depletion mode a negative gate voltage with a particular bias sequence should be applied. In our previous work, we utilized a depletion-mode transistor with a bias sequence to achieve the desired output power. In this paper, we utilized an enhanced mode transistor which needs a positive gate voltage. As a result, a bias control part of Fig. 1 can be eliminated and the reliability of the proposed source can be improved considerably. The proposed structure of the power source is explained in the next section.

## 3 The Proposed RF Source

The block diagram of the proposed structure is shown in Fig. 2. The proposed chain consists of Voltage Controlled Oscillator (VCO), Variable Gain Amplifier (VGA), preamplifier, 90-degree hybrid power combiner, and Doherty power amplifier. As the selected power amplifier

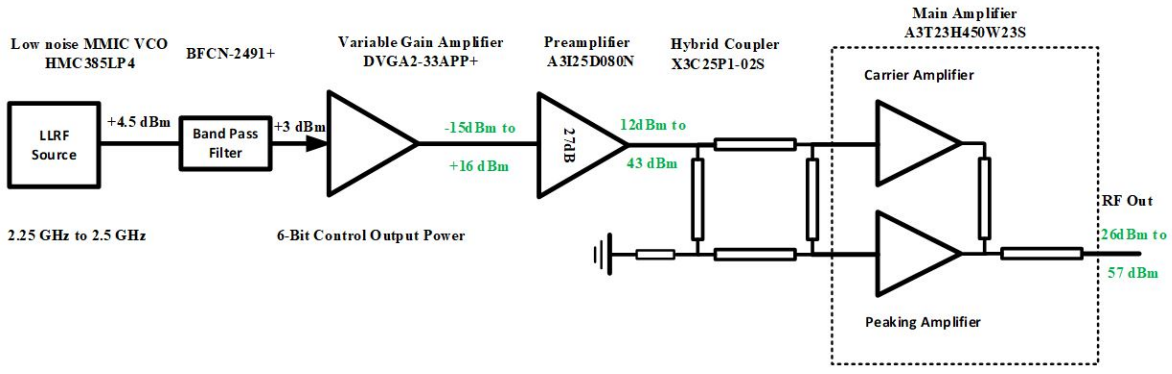


**Figure 2:** Block diagram of the proposed RF high-power source.

does not need negative gate voltage, there is no need to design a bias sequence for it and the source will become more reliable. All part numbers and power limit values are shown in this figure.

Although frequency synthesizers are more stable in the desired working frequency, a voltage-controlled oscillator is selected as the low-level RF source for design simplicity. A monolithic microwave integrated circuit (MMIC) VCO is used with a frequency range of 2.25 to 2.5 GHz. The output power of the VCO is about 4.5 dBm and its supply current is less than 40 mA with 3 V bias voltage. The utilized VCO has output harmonics in which the second and third harmonics are 7 dB and 23 dB lower than the fundamental tone. As a result, a bandpass filter should be added to suppress these harmonics. The utilized filter can reject the second and third harmonics, more than 30 dB. A controllable gain amplifier in cascade with a preamplifier is chosen as a gain stage to drive the main power amplifier. 6-bit digital pins can control the gain value of the first amplifier with a resolution of 0.5 dB. The maximum and minimum attenuation value is obtained as follows:

$$Att = 2^n \times Res \tag{1}$$

where $n$ is the number of bits and $Res$ is the resolution step value. As a result with six control bits, the maximum attenuation value is about 32 dB.

The main power amplifier is Doherty type and is internally matched at both input and output sides. The block diagram of a Doherty amplifier is shown in Fig. 3. An amplitude-modulated input signal is divided into two paths: the envelope of the input signal and its phase. According to Fig. 3, the envelope of the input signal is applied to the carrier amplifier and the phase of the input signal which has a constant envelope is applied to the carrier amplifier. Finally, they are combined, leading to a linear amplification with high power efficiency. As the peaking amplifier can be nonlinear with higher power efficiency, this way is usually used in linear high-efficient applications.

According to the datasheet of the selected Doherty amplifier, the input signal should come from a hybrid power coupler which is depicted in Fig. 2. The utilized hybrid coupler is X3C25F1 which is designed for Doherty applications (X3C25F1-03S, 2022). A schematic of the selected hybrid coupler is shown in Fig. 4. The isolated port of the hybrid coupler is termed to the ground and the other ports are applied to the Doherty amplifier as it is shown in Fig. 2.

A3T23H450W23SR6 which is selected as the high-power transistor has two main advantages (A3T23H450W23S, 2022). The first one is that it does not need any matching network on the input and output sides. As a result, the design will be much simple and more reliable than the block diagram in Fig. 1. The second feature is that as the gate voltage of the selected amplifier is positive, there is no need to utilize sequential circuits for the device start-up procedure.

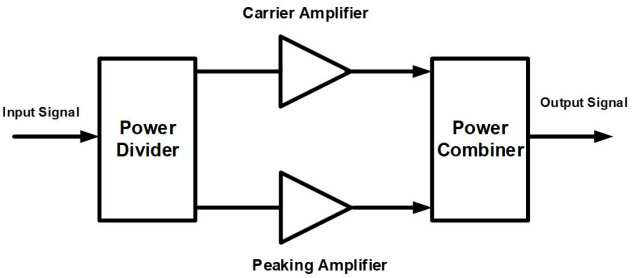


**Figure 3:** Block diagram of a Doherty power amplifier.

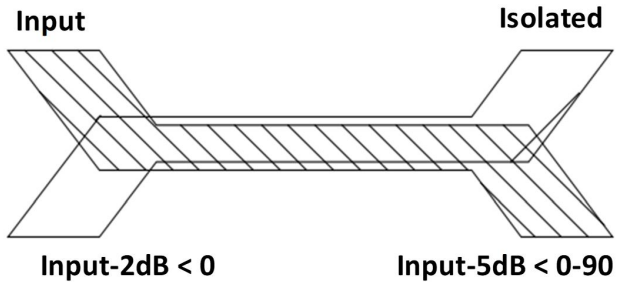


**Figure 4:** Schematic of a hybrid coupler.

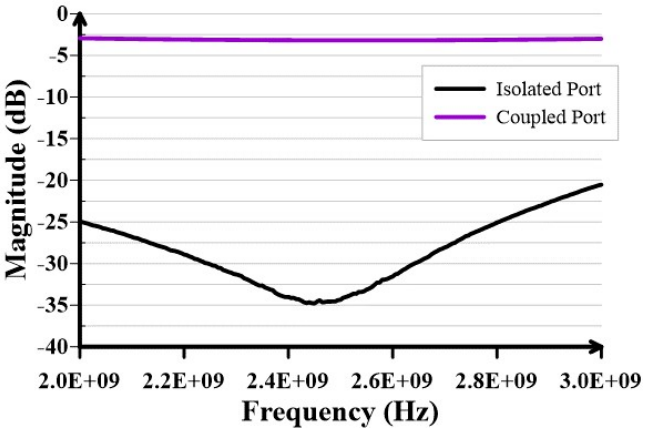


**Figure 5:** Frequency response of the hybrid coupler.

## 4 Results and discussion

The simulations were performed by the momentum RF simulator of the Advanced Design System and the precise and practical model of the components in the S-Band. Rogers RO4350B with a thickness of 20 mils and 3.66 dielectric constants is selected as the substrate of the proposed solid-state source. The output power of VCO is considered +4.5 dBm in simulations and other components are modeled by their measured scattering parameters. The power supply of the Doherty RF transistor is 30 V and some optimization techniques were performed in PCB layout to achieve maximum power and better output return loss.

Figure 5 shows the measured scattering parameters of the utilized hybrid coupler. The isolated port has 35 dB isolation at the center frequency of 2.45 GHz. Also, the coupled ports have 3 dB attenuation and have a 90-degree phase difference.

**Table 1:** Comparison of the proposed power source with other solid-state based works.

| Document | Frequency (GHz) | Power (dBm) | Type | Efficiency (%) | Year |
|---|---|---|---|---|---|
| (Wen et al., 2018) | 2.45 | < 53 | - | - | 2018 |
| (Fatkullin et al., 2018) | 2.4 - 2.5 | <50 | - | - | 2018 |
| (Latrasse et al., 2017) | 2.4 - 2.5 | 0 - 53 | - | <80 | 2017 |
| (Yang et al., 2015) | 1.7 - 2.7 | 52.7 - 54.3 | Doherty | <50 | 2015 |
| (Chen et al., 2017) | 2.7 - 3.1 | <44 | B | <44 | 2017 |
| (Belaïd et al., 2020) | 2.7 - 2.9 | < 45 | AB | <48 | 2020 |
| (Nakatani and Ishizaki, 2015) | 2.4 - 2.5 | 50 | F | <68 | 2015 |
| (Bogomolov et al., 2019) | 2.4 - 2.5 | < 50 | - | - | 2019 |
| (Rahimpour et al., 2022) | 2.4 - 2.5 | 25 - 55 | AB | <70 | 2022 |
| Present study | 2.3 - 2.5 | 25 - 57 | Doherty | <45 | |

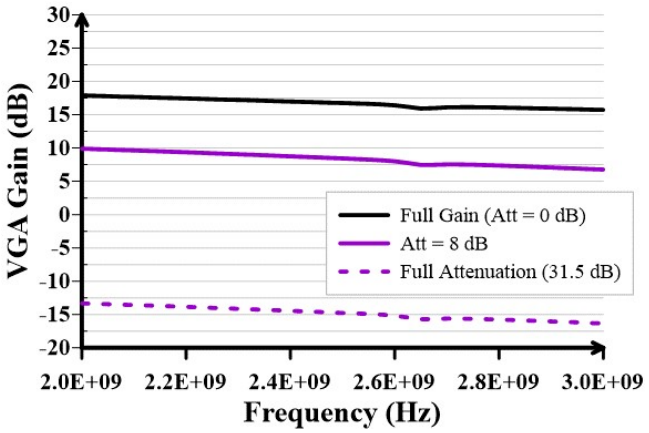


**Figure 6:** Small signal gain of the variable gain amplifier.

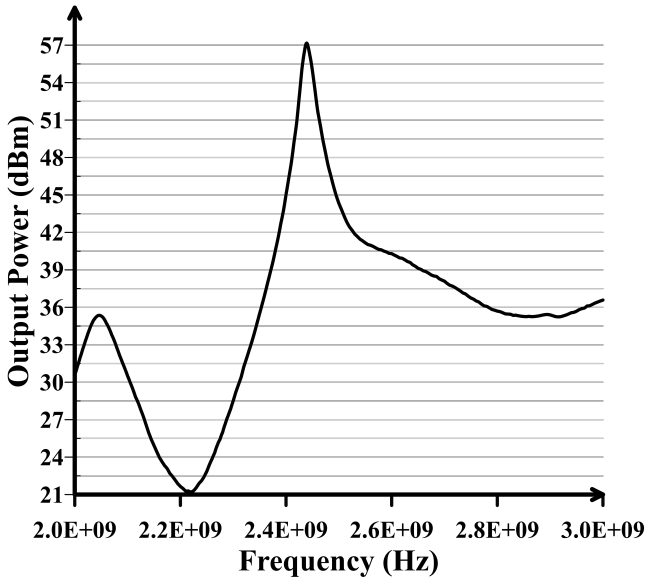


**Figure 7:** The simulated output power of the proposed RF source.

Figure 6 shows the small-signal gain of the variable gain amplifier which is obtained by its scattering parameters matrix. According to this figure, the maximum and minimum gain of the first amplifier can change from 17 dB to -14 dB. As it was explained, the resolution of attenuation is 0.5 dB.

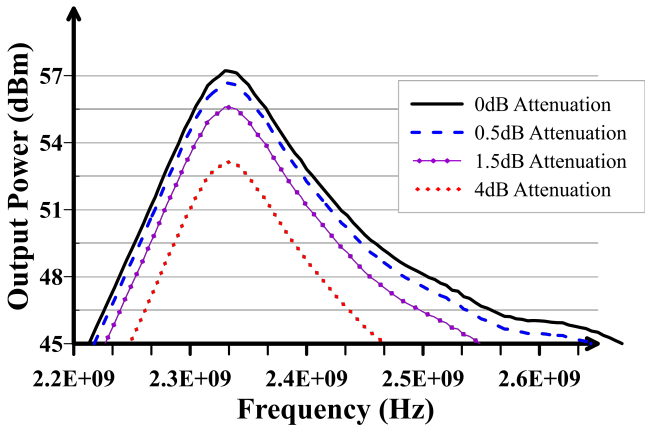


**Figure 8:** Output power of the proposed RF sourc for differe attenuation values.

Figure 7 shows the output power of the proposed RF source in dBm where 53 dBm and 56 dBm stand for 200 W and 400 W, respectively. The output frequency can be easily adjusted by changing the VCO voltage level which can be tuned from 2.1 to 2.5 GHz. The output power of the designed RF source is adjustable by the VGA 6-bit control bits which can be fined tune from 25 to 57 dBm.

The output power of the proposed source for different attenuation values is shown in Fig. 8. The maximum output power is obtained when all six control bits of VGA be pulled down. This state is shown in Fig. 8 by the black line. So other levels of the output power are easily obtainable by changing the value of control bits.

The output return loss frequency response of the proposed RF source is shown in Fig. 9. the bandwidth of the output matching can be optimized by adding a stub to the output side of the Doherty power amplifier. Also, the frequency location of the peak power can be tuned by changing the VCO voltage. The power efficiency of the proposed structure is sufficient because of using a Doherty-type amplifier.

A comprehensive comparison of the proposed structure with other related works is performed and the results are brought in Table 1. 'AB', 'B', and 'F' in Table 1 are different types of power amplifier working classes. The main difference between the proposed structure and our previous work (Rahimpour et al., 2022) is that the main high power transistor is internally matched at both input and

output sides which eliminates designing a matching network. On the other hand, the gate voltage of the power transistor needs positive voltage and there is no need to use a bias sequence circuit.

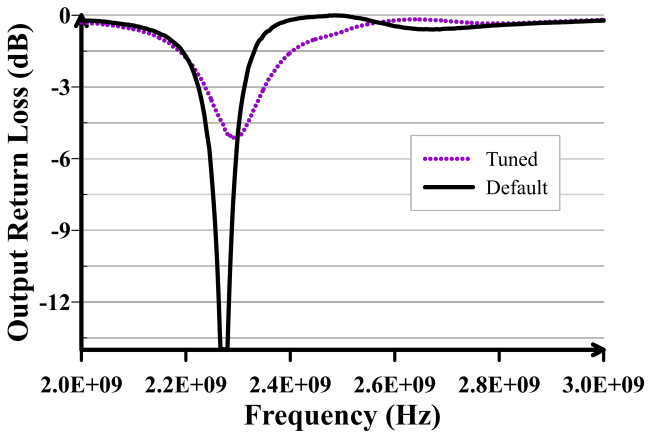


**Figure 9:** The simulated output return loss of the proposed RF source.

## 5 Conclusions

A single transistor-based solid-state power source for ion source application is presented in this paper with the ability of fine-tunable output power and center frequency. The proposed structure can deliver more than 400 W to the miniature ion chamber. The designed RF source has a good power efficiency and is reliable because there is no need to use an external matching network. As the main power transistor is enhancement-type MOSFET, the gate-source voltage should be positive to turn it on and there is no need to use a bias sequence controller. We would try to implement the proposed structure in future works.

## Conflict of Interest

The authors declare no potential conflict of interest regarding the publication of this work.

## Open Access



## References

A3T23H450W23S (2022). A3T23H450W23S|2300-2400 MHz, 87 W Avg, 30 V | NXP Semiconductors.

Belaïd, M. A., Almusallam, A., and Masmoudi, M. (2020). Rf performance reliability of power N-LDMOS under pulsed-RF aging life test in radar application S-band. *IET Circuits, Devices & Systems*, 14(6):805–810.

Bogomolov, S., Bondarchenko, A., Efremov, A., et al. (2019). Development of compact 2.45 GHz ECR ion source for generation of singly charged ions. *Journal of Instrumentation*, 14(01):C01009.

Bondarenko, T., Ilynski, S., Polikhov, S., et al. (2019). Power combining scheme of solid-state RF amplifier. In *Journal of Physics: Conference Series*, volume 1238, page 012075. IOP Publishing.

Chen, X., Chen, W., Zhang, Q., et al. (2017). A 200 watt broadband continuous-mode Doherty power amplifier for base-station applications. In *2017 IEEE MTT-S International Microwave Symposium (IMS)*, pages 1110–1113. IEEE.

Duc, L. H., The, A. N. D., Gia, D. B., et al. (2018). High-power low-loss air-dielectric stripline Gysel divider/combiner for particle accelerator applications at 352 MHz. *The Journal of Engineering*, 2018(5):264–267.

Fatkullin, R., Bogomolov, S., Kuzmenkov, K., et al. (2018). Compact 2.45 GHz ECR Ion Source for generation of singly-charged ions. In *EPJ Web of Conferences*, volume 177, page 08003. EDP Sciences.

Latrasse, L., Radoiu, M., Nelis, T., et al. (2017). Self-matching plasma sources using 2.45 GHz solid-state generators: microwave design and operating performance. *Journal of Microwave Power and Electromagnetic Energy*, 51(4):237–258.

Nakatani, K. and Ishizaki, T. (2015). A 2.4 GHz-band 100 W GaN-HEMT high-efficiency power amplifier for microwave heating. *Journal of Electromagnetic Engineering and Science*, 15(2):82–88.

Piel, C., Aminov, B., Borisov, A., et al. (2005). Development of a Solid State RF Amplifier in the KW Regime for Application with Low Beta Superconducting RF Cavities. In *Proceedings of the 2005 Particle Accelerator Conference*, pages 1–3. IEEE.

Rahimpour, H., Mirzaei, H., and Yarmohammadi Satri, M. (2022). Analysis and design of a 2.45 GHz RF power source for a miniature electron cyclotron resonance ion source (Accepted manuscript). *Radiation Physics and Engineering*.

Tuo, W., Hongyi, C., and Dahong, Q. (2009). Theoretical analysis and an improvement method of the bias effect on the linearity of RF linear power amplifiers. *Journal of Semiconductors*, 30(5):055002.

Wen, J.-M., Peng, S.-X., Ren, H.-T., et al. (2018). A miniaturized 2.45 GHz ECR ion source at Peking University. *Chinese Physics B*, 27(5):055204.

X3C25F1-03S (2022). X3C25F1-03S Anaren Microwave - Distributors and Price Comparison | Octopart Component Search.

Yang, Y., Zhang, M., Che, W., et al. (2015). High power S-band GaN-based power amplifier for radar systems. In *2015 IEEE MTT-S International Microwave Workshop Series on Advanced Materials and Processes for RF and THz Applications (IMWS-AMP)*, pages 1–3. IEEE.

RPE | Radiation Physics & Engineering
An International Peer-Reviewed Journal
Published by K.N. Toosi University of Technology
http://rpe.kntu.ac.ir
Research Article

Radiation Physics and Engineering 2022; 3(4):7–15
https://doi.org/10.22034/rpe.2022.323131.1050

# Determination of TG-43 dosimetric parameters for I-125, Ir-192, and Co-60 brachytherapy sources using the Monte Carlo simulation

Milad Payandeh[a], Mahdi Sadeghi[a,*], Dylan Richeson[b], Somayeh Gholami[b]

[a] *Medical Physics Department, School of Medicine, Iran University of Medical Sciences, P.O. Box: 14155-6183, Tehran, Iran*
[b] *Department of Radiation Oncology, Virginia Commonwealth University, Richmond, VA 23219, USA*

## HIGHLIGHTS

- Dose rate constant was obtained for I-125, Ir-192 and Co-60 brachytherapy sources using MCNP5 code.
- Radial dose function parameter $g(r)$ was obtained for I-125, Ir-192, and Co-60 using MCNP5 code.
- Anisotropy function $F(r,\theta)$ was obtained for I-125, Ir-192, and Co-60 using MCNP5 code.
- All calculated parameters for I-125, Ir-192 and Co-60 brachytherapy sources were in consistent with reference studies.

## ABSTRACT

It is important to have accurate information regarding the dose distribution for treatment planning and to accurately deposit that dose in the tissue surrounding the brachytherapy source. However, the practical measurement of dose distribution for various reasons is associated with several problems. In this study, 6711 I-125, Micro Selectron mHDR-v2r Ir-192, and Flexisource Co-60 sources were simulated using the MCNP5 Monte Carlo method. To simulate the sources, the exact geometric characteristics of each source, the material used in them, and the energy spectrum of each source were entered as input to the program, and finally, the dosimetric parameters including dose rate constant, radial dose function, and anisotropy function were calculated for considered seeds according to AAPM, TG-43 protocol recommendation. Results obtained for dosimetric parameters of dose rate constant, radial dose function, and anisotropy function for I-125, Ir-192, and Co-60 sources agreed with other studies. According to the good agreement obtained between the parameters of TG43 and other studies, now these datasets can be used as input in the treatment planning systems and to validate their calculations.

## KEYWORDS

Brachytherapy
Dosimetric parameters
TG-43 protocol
Monte Carlo simulation
MCNP5 code

## HISTORY

Received: 4 January 2022
Revised: 12 May 2022
Accepted: 20 June 2022
Published: Autumn 2022

## 1 Introduction

Brachytherapy is a form of internal radiation therapy in which a radioactive source is placed within or near the target. This proximity allows the dose to be concentrated while minimizing exposure to surrounding healthy tissue (DeMarco et al., 1998; Cross et al., 2003).

This method plays an important role in the treatment of cancers related to different organs such as the head and neck, brain, prostate, cervix, vagina, and breast, in which it is possible to enter or implant the radioactive sources (Huh et al., 2007; Mostaar et al., 2003). Therefore, accurate information about the dose distributions is an important factor in treatment planning. As a result, to control and destroy cancer cells as well as minimize damage to the surrounding healthy tissues, dosimetric calculations must be performed with great precision. On the other hand, the practical measurement of the dose often faces several challenges such as the lack of clarity of the dose report due to the large size of common dosimeters, the energy dependence of these dosimeters, lack of tissue equivalent material in detectors, etc. (Williamson et al., 1998). One way to calculate the parameters, approved by the AAPM, is to calculate the dose distribution in water using the Monte Carlo method.

In 1998, The American Association of Physicists in Medicine (AAPM) noted that before the use of different sources in brachytherapy, their dosimetric parameters were determined by Monte Carlo calculations at least once in daily medical applications (Rivard et al., 2004). Therefore, in the present study, the mentioned parameters for I-125, Ir-192, and Co-60 sources were calculated using the MCNP5 code.

Ir-192 is a convenient source for use in brachytherapy.

*Corresponding author: sadeghi.m@iums.ac.ir

This source is made in the form of thin flexible wires that can be cut to any length (IAEA, 2000; Kacperek, 2000). The malleability and flexibility of this source provide the possibility to be produced in different dimensions and thicknesses.

Additionally, I-125 is a suitable material for permanent implantation in radiotherapy (Urie et al., 1984). The advantage of I-125 is that it requires less shielding due a lower photon energy compared the gold source.

Co-60 can also be used for brachytherapy. The main advantage of Co-60 is its high specific activity rate allowing it to be constructed with small dimensions for some specific applicators.

The purpose of this study is to obtain the dosimetric parameters for the 6711 I-125, Micro Selectron mHDR-v2r Ir-192, and Flexisource Co-60 sources using the MCNP5 code. The advantage and innovation of this research compared to similar research are that we perform the calculations of dosimetric parameters for three sources at the same time and therefore it can provide a suitable source for the validation of these sources for researchers.

## 2 Materials and methods

In this study, two high dose rate model sources, Flex source Co-60 and Micro Selectron mHDR-v2r Ir-192, as well as a low dose rate source 6711 I-125 were simulated using Monte Carlo code. Dose distributions in this work were simulated with the MCNP5 radiation transport code published by Los Alamos National Laboratory (MCNP5, 2008). In the simulation process, the exact geometric characteristics of the sources, the materials used in each part of the seeds, and the energy spectrum of the particles emitted by the sources should be exactly modeled.

The first source studied in the present study is the 6711 I-125 source, which is shown in Fig. 1. In the design process, there is a silver cylindrical marker with a density of 10.5 g.cm$^{-3}$, a length of 2.8 mm, and a radius of 0.2 mm covered with a combination of silver iodide (AgI) with a density of 6.2 g.cm$^{-3}$ and a thickness of 2 $\mu$m. The seed is placed in a titanium capsule with a density of 4.54 g.cm$^{-3}$ and its ends are bounded on both sides by a hemisphere. The average energy of the I-125 source is equal to 280 keV, and its half-life is about 60 d (Rivard, 2009). Also, the photon spectrum of the 6711 I-125 source used in this study according to TG-43 and AAPM reports is shown in Table 1 (Rivard et al., 2004).

The second source used is the Micro Selectron mHDR-v2r Ir-192 its primary material includes enriched iridium and has dimensions of 3.5 mm in length and 0.6 mm in diameter with an effective density of 22.42 g.cm$^{-3}$. This radioisotope is covered with a layer of air with a specific thickness on each side, and the inside of the tube is made of AISI 316L stainless steel with a density of 3.03 g.cm$^{-3}$ with a diameter of about 0.9 mm. One end of the tube is blocked by laser welding and the other end is connected to a steel cable of an AISI 304L stainless steel with a density of 4.88 g.cm$^{-3}$. The cable length is considered to be 2 mm in the Monte Carlo simulation, which is practically longer and is also called a guidewire. The diameter of this cable is 0.7 mm and as shown in Fig. 2, its starting point is 1.185 mm away from the source. The average energy of this source is 380 keV and the energy spectrum of the emitting photons is given in Table 2 (López et al., 2011).

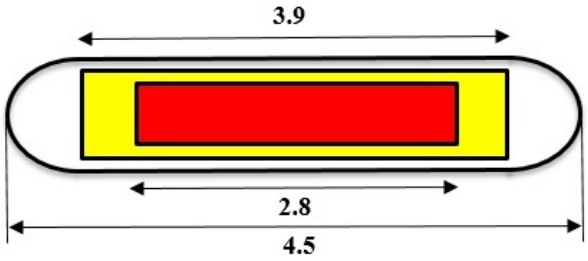


**Figure 1:** Simulation of 6711 I-125 sources in MCNP5 code (values are written in mm. The diameter of the central core, the chamber containing the air, and the titanium chamber are 0.4, 0.66, and 0.8 mm, respectively)

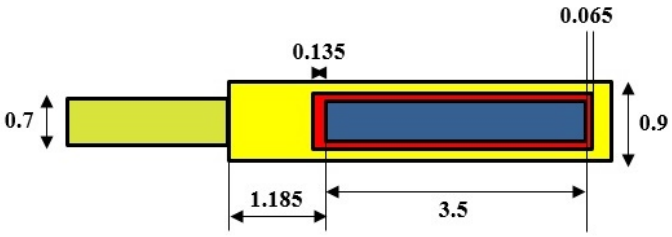


**Figure 2:** Simulation of Ir-192 source in MCNP5 code (values are written in mm. The internal and external diameters of the source are 0.6 and 0.7 mm).

**Table 1:** Photon spectrum of I-125 source according to TG-43 and AAPM report.

| Photon energy (keV) | Intensity (%) |
|---|---|
| 27.202 | 40.6 |
| 27.472 | 75.7 |
| 30.98 | 20.2 |
| 31.71 | 4.39 |
| 35.492 | 6.68 |

**Table 2:** Photon spectrum of Ir-192 source.

| Photon energy (keV) | Intensity (%) |
|---|---|
| 9.44 | 1.47 |
| 11.07 | 1.24 |
| 61.49 | 1.2 |
| 63 | 2.07 |
| 65.12 | 2.65 |
| 66.83 | 4.53 |
| 75.75 | 1.03 |
| 205.8 | 3.3 |
| 295.96 | 28.67 |
| 308.46 | 0.3 |
| 316.51 | 82.81 |
| 468.07 | 47.83 |
| 484.58 | 3.18 |
| 588.58 | 4.52 |
| 604.41 | 8.23 |
| 612.47 | 5.31 |

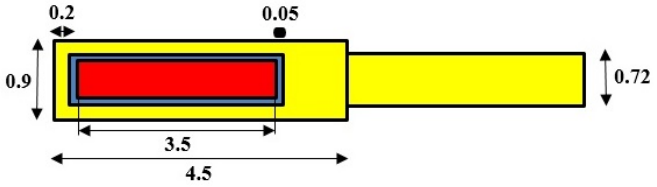


**Figure 3:** Simulation of Co-60 source in MCNP5 code (values are written in mm. The internal and external diameters of the source are 0.5 and 0.6 mm).

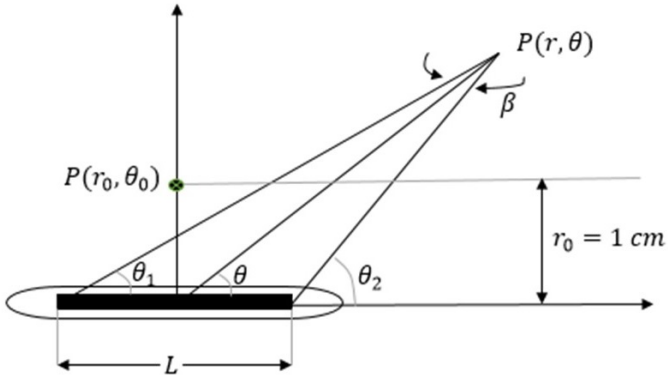


**Figure 4:** The coordinate system and the parameters used for brachytherapy dosimetry calculations.

**Table 3:** Photon spectrum of Co-60 source.

| Photon energy (keV) | Intensity (%) |
|---|---|
| 347.14 | 0.0075 |
| 826.10 | 0.0076 |
| 1173.23 | 99.85 |
| 1332.49 | 99.9826 |
| 2158.57 | 0.0012 |
| 2505.69 | 0.000002 |

Finally, the design and dimensions of the simulated Flexisource Co-60 source are shown in Fig. 3. This seed consists of an active cylindrical metal core of Co-60 with a density of 8.95 g.cm$^{-3}$, a length of 3.5 mm, and a diameter of 0.5 mm surrounded by a layer of air with a thickness of 0.5 mm. The set is covered with AISI 316L stainless steel with a diameter of 0.9 mm. Also in the present study, we have considered a cable with a length of 5 mm of AISI 316L with an effective density of 3.81 g.cm$^{-3}$ and a diameter of 0.72 mm at the end of the seed. The average energy of this source is 1.525 MeV and its half-life is about 5.26 years. The long half-life of Co-60 makes it a concern for use in brachytherapy. To remedy this, physicians use temporary implants which are removed when the prescribed dose has been reached. The range of energy used in this simulation is given in Table 3 (Vijande et al., 2012). Finally, the physical details and distances of the three sources are shown in Table 4.

AAPM has introduced a dose calculation method to calculate the distribution of 2D doses around symmetrical cylindrical sources. For each source, the dose distribution can be expressed in terms of a polar coordinate system where the origin corresponds to the source center at a distance $r$ from the center to the desired point and angle relative to the longitudinal axis of the source. The point $p(r_0, \theta_0)$ is the reference point on the vertical semicircle of the source at a distance of one centimeter from the source ($r_0 = 1$ cm, $\theta_0 = \pi/2$). The general, 2D dose rate formula from the 1995 TG-43 protocol is given in Eq. (1) (Rivard et al., 2004). Besides, the coordinate system and the parameters used for brachytherapy dosimetry calculations are introduced in Fig. 4.

$$\dot{D}(r,\theta) = S_K \Lambda \frac{G_L(r,\theta)}{G_L(r_0,\theta_0)} g_L(r) F(r,\theta) \tag{1}$$

In Eq. (1), $G_L(r,\theta)$, $g_L(r)$, and $F(r,\theta)$ are the geometry function, radial dose function, and anisotropy function, respectively. The geometry function $G_L(r,\theta)$ is normalized to a point 1 cm from the source center along a perpendicular bisector. Its purpose is to quantify the effect of the spatial arrangement of radioactive material on the dose distribution.

The radial dose function, $g(r)$, indicates the effects of photon scattering, the attenuation in water, and dose fall-off on the transverse plane ($\theta_0 = \pi/2$). The radial dose function is defined according to Eq. (2) (Rivard et al., 2004):

$$g(r) = \frac{\dot{D}(r,\theta_0)}{\dot{D}(r_0,\theta_0)} \frac{G_L(r_0,\theta_0)}{G_L(r,\theta_0)} \tag{2}$$

where $\dot{D}(r,\theta_0)$ and $G_L(r,\theta_0)$ are dose rate and geometry function, respectively.

The 2D anisotropy function, $F(r,\theta)$, expresses the angular changes of the dose rate related to seeds at each distance and depends on the intrinsic filtration, the initial filtration of the primary photons passing through the capsule containing the source, and the rate of photon absorption and scattering in the surrounding medium. The 2D anisotropy function is defined according to (Rivard et al., 2004):

$$F(r,\theta) = \frac{\dot{D}(r,\theta)}{\dot{D}(r,\theta_0)} \frac{G_L(r,\theta_0)}{G_L(r,\theta)} \tag{3}$$

The air-Kerma strength ($S_K$) expresses the intensity of the source used in brachytherapy ($K$) which should be located on the transverse plane in free space and at a certain distance ($d$) from the center of the source by the Eq. (4). $S_K$ is represented by the air-Kerma unit (U), where 1 U=1 $\mu$Gym$^2$.h$^{-1}$=1 cGycm$^2$.h$^{-1}$ (Rivard et al., 2004):

$$S_K = \dot{K}_\delta(d) d^2 \tag{4}$$

Dose rate constant, $\Lambda$, is the ratio of dose rate in the water at a distance of 1 cm from the source geometric center on the transverse plane and $S_K$ obtained from Eq. 3. Its unit is cGy.h$^{-1}$/cGy.m$^2$.h$^{-1}$=cGy.h$^{-1}$.U$^{-1}$ (Nath, 1995):

$$\Lambda = \frac{\dot{D}(r_0,\theta_0)}{S_K} \tag{5}$$

To calculate the absorbed dose rate in cGy.s$^{-1}$, the following general rule can be applied to each seed (Alizadeh

**Table 4:** Physical details and distances of sources.

| Source | Density (g.cm$^{-3}$) | Average energy (MeV) | Half-life (Days) | Length (mm) | Diameter (mm) |
|---|---|---|---|---|---|
| I-125 | 10.5 | 0.28 | 60 | 2.8 | 0.4 |
| Ir-192 | 22.42 | 0.38 | 74 | 3.5 | 0.6 |
| Co-60 | 8.95 | 1.525 | 1920 | 3.5 | 0.5 |

**Table 5:** Results of the dose rate constant parameter for 6711 I-125 source, micro Selectron mHDR-v2r Ir-192 source, and Flexisource Co-60 sources and comparison with Dolan, López, Vijande's results.

| The source under study | This Work | $\Lambda$ (cGy.H$^{-1}$U$^{-1}$) Comparative Article | | Difference (%) |
|---|---|---|---|---|
| I-125 6711 | $0.949 \pm 0.001$ | (Dolan et al., 2006) | 0.942 | 0.8 |
| Ir-192 mHDR-v2r | $1.109 \pm 0.001$ | (López et al., 2011) | 1.112 | 0.3 |
| Co-60 Flexisource | $1.083 \pm 0.001$ | (Vijande et al., 2012) | 1.085 | 0.18 |

et al., 2015):

$$\begin{aligned} &\text{Dose rate (cGy.s}^{-1}) = \\ &\text{MC output (MeV.g}^{-1}\text{ per photon)} \\ &\times 10^{6}\text{ eV.MeV}^{-1} \times 1.602 \times 10^{-19}\text{ J.eV}^{-1} \\ &\times 10^{3}\text{ g.kg}^{-1}\text{ amount of decay per s (Ci)} \\ &\times 3.7 \times 10^{10}\text{ Bq.Ci}^{-1} \\ &\times \#\text{ photon.dis}^{-1} \times 1\text{ dis.s}^{-1}\text{Bq}^{-1} \end{aligned} \tag{6}$$

According to Eq. (5), to calculate the dose rate constant, two parameters of absorption dose and kerma strength must be calculated for these seeds. For this purpose, according to Eq. (4), the air-kerma strength was calculated first at a distance of one meter and perpendicular to the seed axis ($\theta_0 = 90$). The source was then placed in a vacuum sphere with the center of the coordinate system in the center of the core and the air-kerma was calculated inside the volume enclosed by spherical shells with a radius of 99.5 and 100.5 cm and a cone with a vertex angle of 10° (between two cones with vertex angles of 85 and −85°) using the F6 tally. (The desired cell is approximately located at a distance of one meter and at an angle perpendicular to the source plane) (Rivard, 2009). Thereafter the air-kerma rate can be achieved by multiplying the air-kerma value by the amount of activity of the source and the number of photons in each decay as well as a constant value given in equation 6. In the second step, to calculate the value of the dose rate at the reference point ($r_0 = 1cm, \theta_0 = 90°$) we consider a water sphere with a radius of 15 cm and place the radioactive seed in the center of this sphere. To measure the absorbed dose, a volume enclosed by spherical shells with a radius of 0.95 and 1.05 cm and a cone with a vertex angle of 10° is assumed and calculated using the F6 tally (Sadeghi et al., 2008b), and finally, the dose rate was obtained using the Eq. (6) (Sadeghi and Hosseini, 2010). It is important to mention that due to the low source energy and the short range of the secondary electrons produced by the photons emitted through this source, the transfer of secondary electrons was not simulated and the Kerma was considered equal to the dose (assuming an electronic equilibrium). Now according to Eq. (5), the dose rate constant value is calculated for the I-125 Ir-192 and Co-60 sources.

To obtain the radial dose function according to Eq. (2), the value of the absorption dose rate and the $G_L(r,\theta)$ must be calculated using the Monte Carlo simulation. For this purpose, a brachytherapy seed was placed in the center of the sphere with a radius of 15 cm. To calculate the dose rate at different distances (and at a reference angle of 90°) we assumed a sphere of water and used concentric rings with different thicknesses and conical shells with angles of +85° and −85° and obtained different values of absorbed dose using F6 tally (Saidi et al., 2010). Conical shells were selected to create 90-degree angles at different distances. The $G_L(r,\theta)$ was also determined by the F4 tally at different distances (and at the reference angle of 90°). To exactly determine the $G_L(r,\theta)$, all the materials used in the seed and its surroundings were assumed to be a vacuum and there was no absorption and scattering in the seed and the ambiance. The value of $g(r)$ was measured at different distances and at a reference angle of 90° (Sadeghi et al., 2008a).

Finally, to measure the anisotropy function according to Eq. (3), the value of the dose rate and the $G_L(r,\theta)$ must be calculated at different distances and angles. For this purpose, the brachytherapy seed was placed in the center of the hypothetical sphere (with a density of 0) with a radius of 15 cm.

In the simulation, a high number of particles (about $10^7$ photons) was used to achieve a standard deviation of less than 0.2% except along the longitudinal axis where 1% was reached.

The dosimetric parameters obtained for I-125, Ir-192, and Co-60 sources were then compared with the Dolan (Dolan et al., 2006), López (López et al., 2011), and Vijande's (Vijande et al., 2012) works and verified the validation of the present simulation.

## 3 Results

The $\Lambda$ parameters for I-125, Ir-192, and Co-60 sources are respectively listed in Table 5, and they are compared with the values obtained in Dolan, López, and Vijande's publications to the validation of the simulation performed.

Also, the radial dose function parameter $g(r)$ for these three sources was obtained in two steps by calculating the absorbed dose and $G_L(r,\theta)$ using Monte Carlo simulation, according to Eq. (2) and using two F6 tally and F4 tally. The parameter $g(r)$ measured for the I-125, Ir-192, and Co-60 sources at various distances with a known reference angle of 90° are shown in Figs. 5, 6, and 7 respectively and are compared with the Dolan, López, and Vijande's works.

The $F(r,\theta)$ anisotropy function was also obtained for the validation of seeds. This function was measured for the I-125 source at distances of 0.5, 1, 2, 3, 4, and 5 cm and angles of 0, 10, 20, 30, 40, 50, 60, 70, 80, and 90°, for the Ir-192 source at distances of 1, 5, 10, and 15 cm and angles of 30, 60, 120, and 150°, and the Co-60 source at distances of 0.5, 1, 2, 3, 4, and 5 cm and angles of 0, 5, 10, 20, 30, 40, 50, 60, 70, 80, and 90°, and the results were presented in Figs. 8 to 23, respectively, to compare with Dolan, López, and Vijande's works.

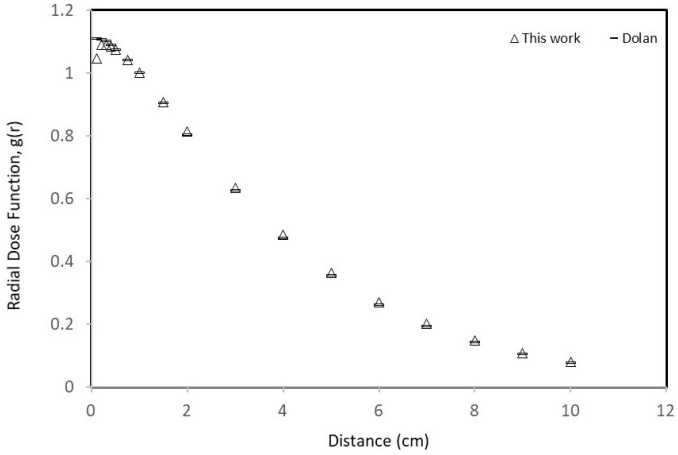


**Figure 5:** The curve of the radial dose function of 6711 I-125 source, calculated with MCNP5 code and comparison with Dolan's (Dolan et al., 2006) results.

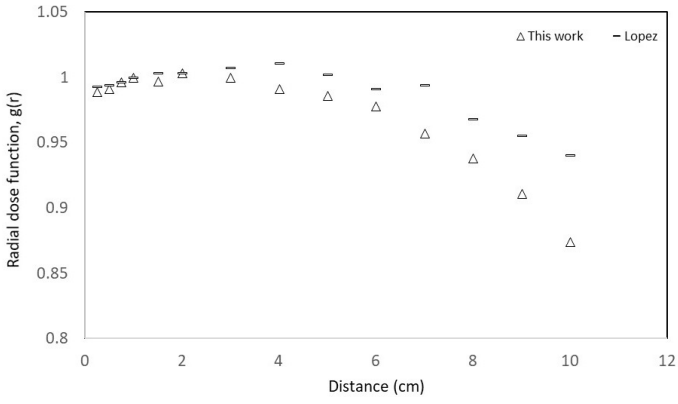


**Figure 6:** The curve of the radial dose function for micro Selectron mHDR-v2r Ir-192 source and comparison with López's (López et al., 2011) results.

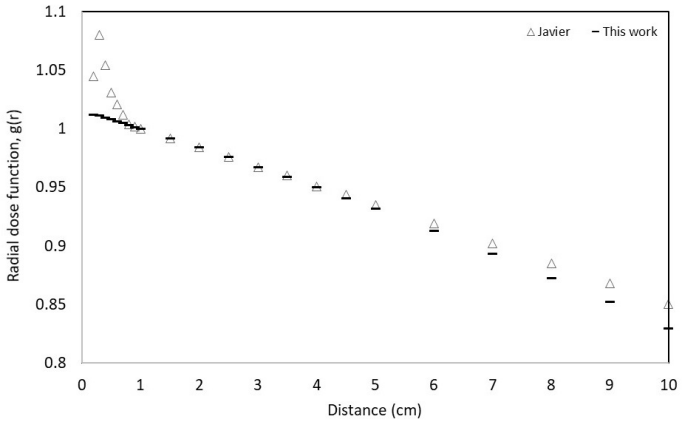


**Figure 7:** The curve of the radial dose function for Flexisource Co-60 source and comparison with Vijande's (Vijande et al., 2012) results.

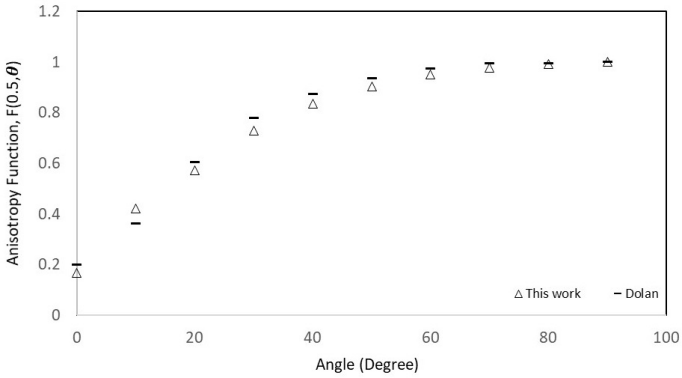


**Figure 8:** Anisotropy function for 6711 I-125 sources, calculated with MCNP5 code at a distance of 0.5 cm and different angles and comparison with the Dolan's (Dolan et al., 2006) results.

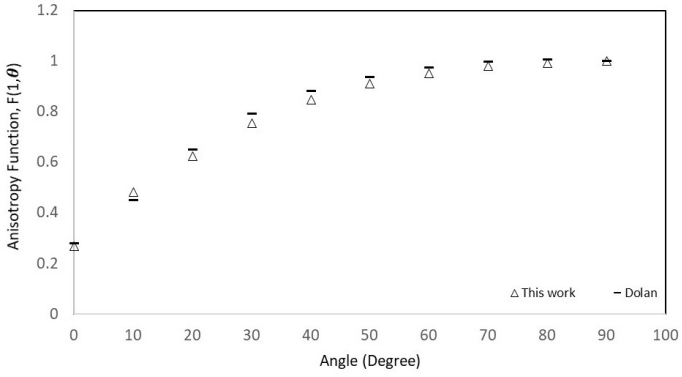


**Figure 9:** Anisotropy function for 6711 I-125 sources, calculated with MCNP5 code at a distance of 1 cm and different angles and comparison with the Dolan's (Dolan et al., 2006) results.

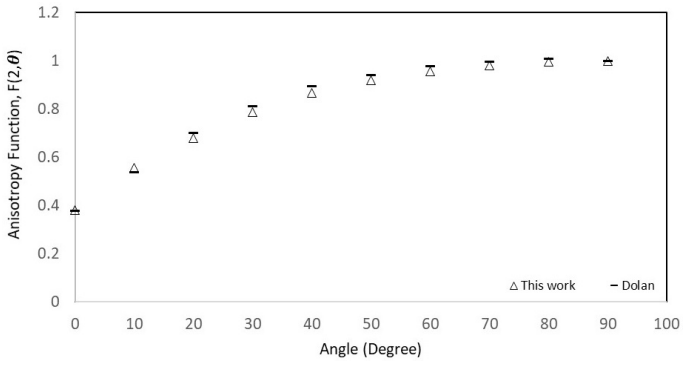


**Figure 10:** Anisotropy function for 6711 I-125 sources, calculated with MCNP5 code at a distance of 2 cm and different angles and comparison with the Dolan's (Dolan et al., 2006) results.

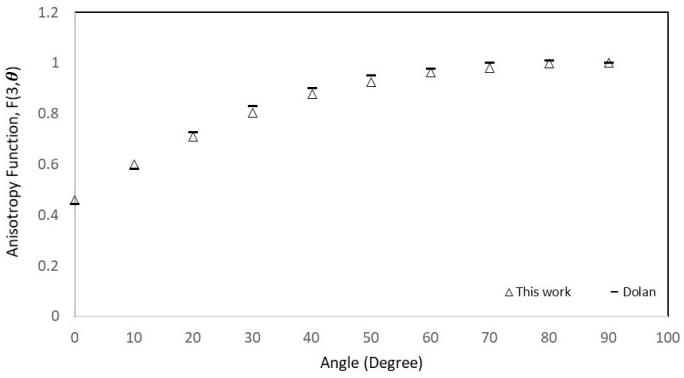


**Figure 11:** Anisotropy function for 6711 I-125 sources, calculated with MCNP5 code at a distance of 3 cm and different angles and comparison with the Dolan's (Dolan et al., 2006) results.

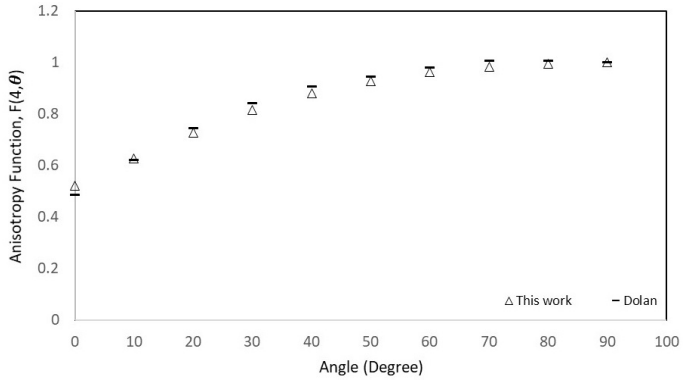


**Figure 12:** Anisotropy function for 6711 I-125 sources, calculated with MCNP5 code at a distance of 4 cm and different angles and comparison with the Dolan's (Dolan et al., 2006) results.

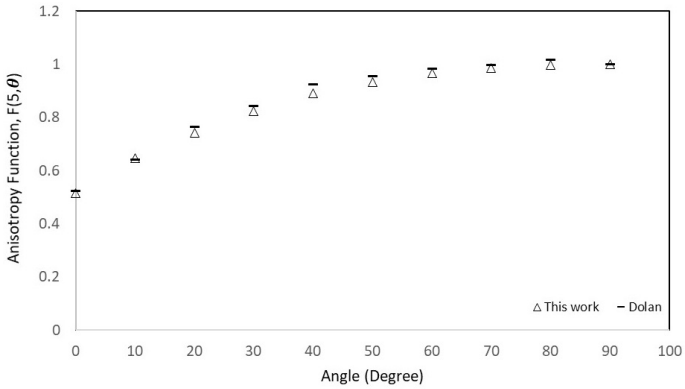


**Figure 13:** Anisotropy function for 6711 I-125 sources, calculated with MCNP5 code at a distance of 5 cm and different angles and comparison with the Dolan's (Dolan et al., 2006) results.

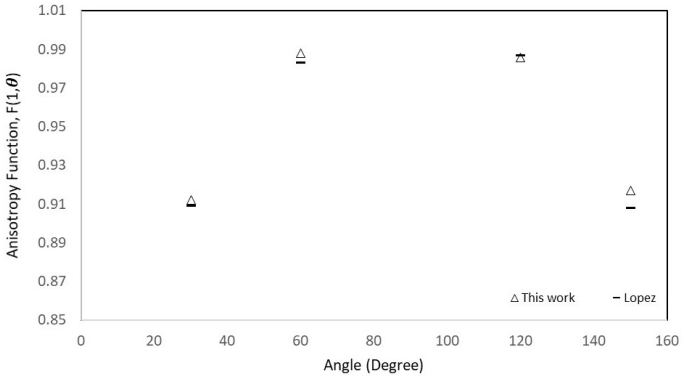


**Figure 14:** Anisotropy function for micro Selectron mHDR-v2r Ir-192 source, calculated with MCNP5 code at a distance of 1 cm and different angles and comparison with López's (López et al., 2011) results.

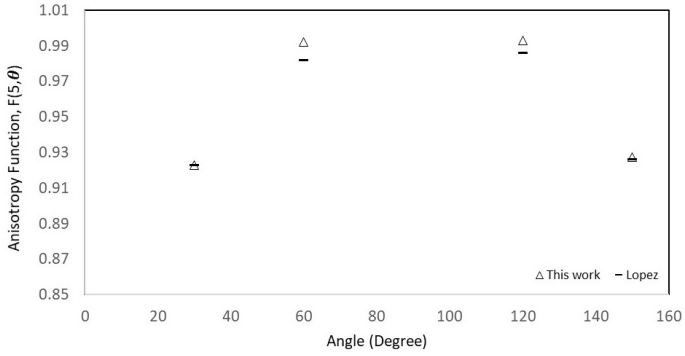


**Figure 15:** Anisotropy function for micro Selectron mHDR-v2r Ir-192 source, calculated with MCNP5 code at a distance of 5 cm and different angles and comparison with López's (López et al., 2011) results.

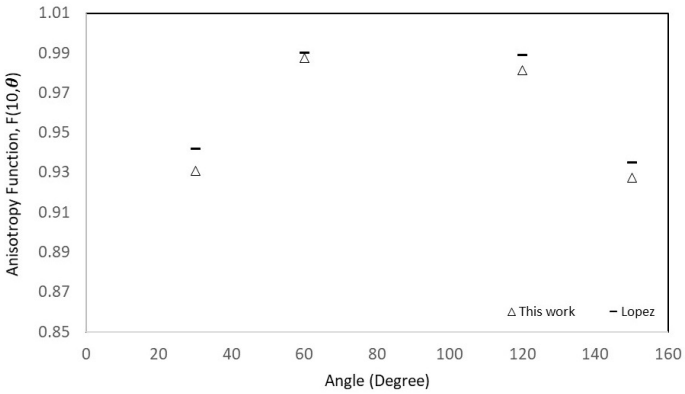


**Figure 16:** Anisotropy function for micro Selectron mHDR-v2r Ir-192 source, calculated with MCNP5 code at a distance of 10 cm and different angles and comparison with López's (López et al., 2011) results.

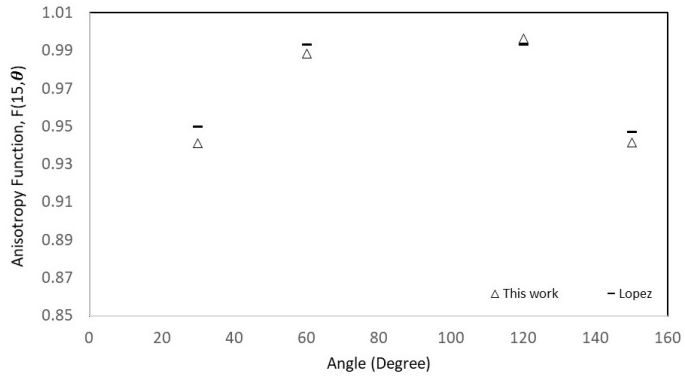


**Figure 17:** Anisotropy function for micro Selectron mHDR-v2r Ir-192 source, calculated with MCNP5 code at a distance of 15 cm and different angles and comparison with López's (López et al., 2011) results.

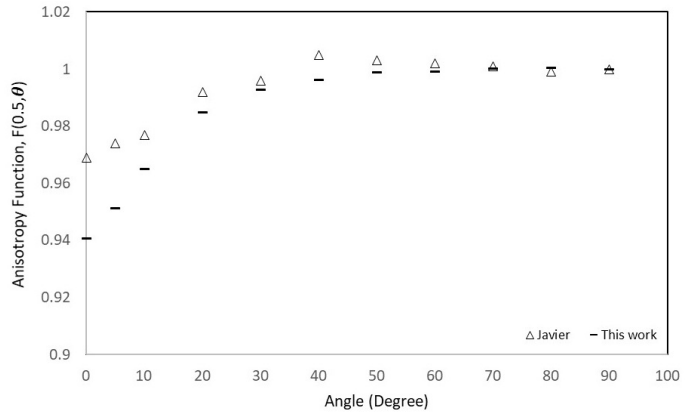


**Figure 18:** Anisotropy function for Flexisource Co-60 source, calculated with MCNP5 code at a distance of 0.5 cm and different angles and comparison with Vijande's (Vijande et al., 2012) results.

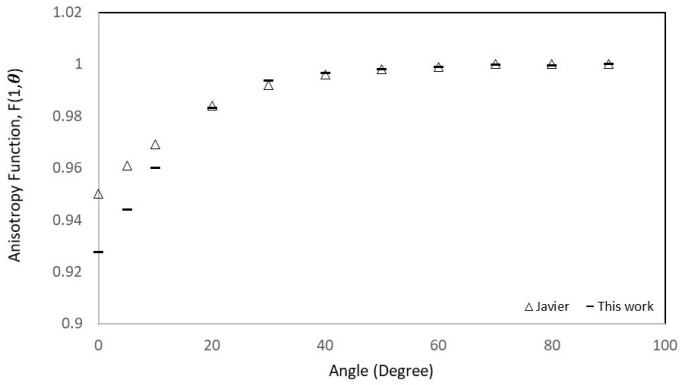


**Figure 19:** Anisotropy function for Flexisource Co-60 source, calculated with MCNP5 code at a distance of 1 cm and different angles and comparison with Vijande's (Vijande et al., 2012) results.

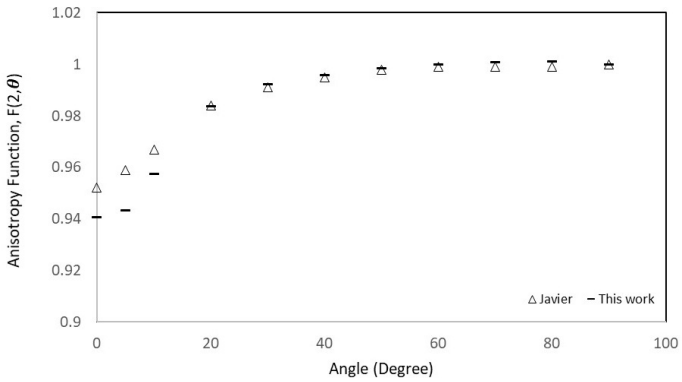


**Figure 20:** Anisotropy function for Flexisource Co-60 source, calculated with MCNP5 code at a distance of 2 cm and different angles and comparison with Vijande's (Vijande et al., 2012) results.

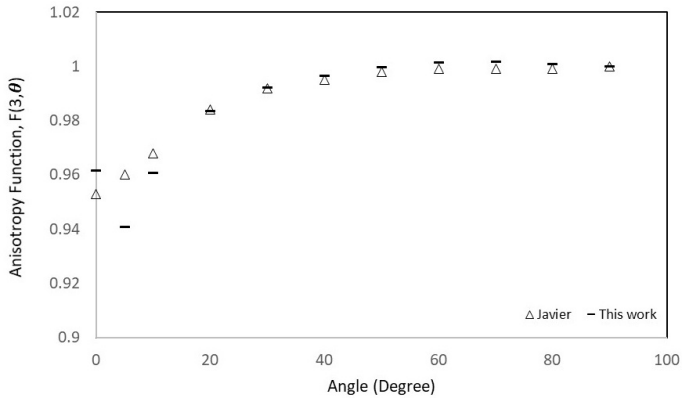


**Figure 21:** Anisotropy function for Flexisource Co-60 source, calculated with MCNP5 code at a distance of 3 cm and different angles and comparison with Vijande's (Vijande et al., 2012) results.

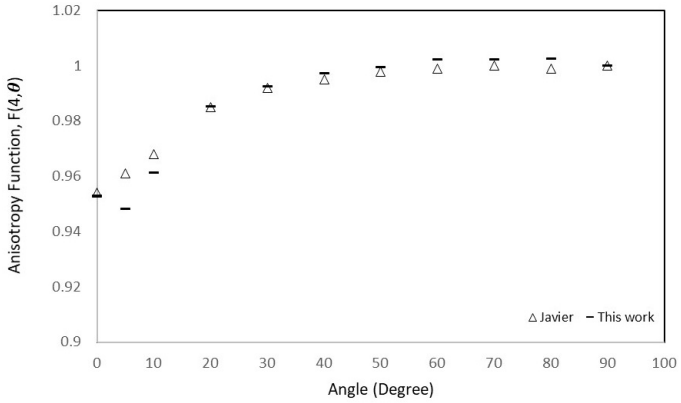


**Figure 22:** Anisotropy function for Flexisource Co-60 source, calculated with MCNP5 code at a distance of 4 cm and different angles and comparison with Vijande's (Vijande et al., 2012) results.

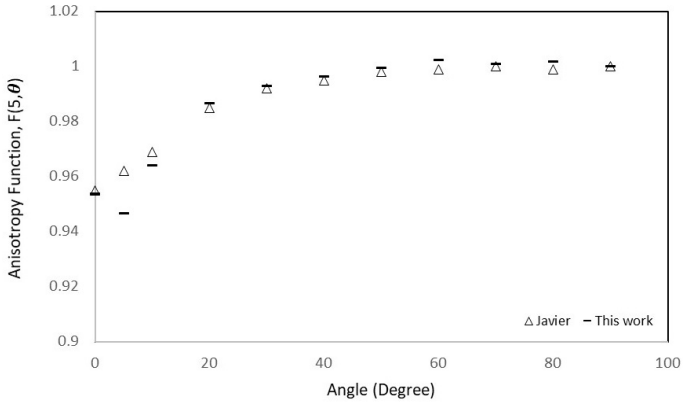


**Figure 23:** Anisotropy function for Flexisource Co-60 source, calculated with MCNP5 code at a distance of 5 cm and different angles and comparison with Vijande's (Vijande et al., 2012) results.

## 4 Discussion

According to Table 5, the dose rate constant value for 6711 I-125 seed, Micro Selectron mHDR-v2r Ir-192 seed, and Flexisource Co-60 seed were $0.949 \pm 0.001$, $1.109 \pm 0.001$ and $1.083 \pm 0.001$ cGy.h$^{-1}$/cGy.m$^2$.h$^{-1}$ respectively, which was inconsistent with Dolan (Dolan et al., 2006), López (López et al., 2011), and Vijande's (Vijande et al., 2012) articles (differences of 0.8%, 0.3%, and 0.18%, respectively).

Figures 5, 6, and 7 demonstrated the comparison of the data related to the Radial dose function g(r) with the data obtained from the above-mentioned studies. In model 6711 I-125 seed, as shown in Fig. 5, the main difference between the measured values and Dolan's data occurred at a short distance from the source (0.1 cm) (about 5%). Moreover, with increasing distance from the source, the difference became less prominent leading to a good agreement with Dolan's data. In addition, for the Micro Selectron mHDR-v2r Ir-192 seed, as shown in Fig. 6, the difference in the value of $g(r)$ between the calculations in the present study and López article, indicated an acceptable agreement at distances less than 3 cm (difference less than 0.7%). However, the discrepancies increase with increasing distance from the source up to a maximum difference of approximately 7% at 10 cm from the source. Comparing the $g(r)$ parameter between the present study and Vijande's article, as shown in Fig. 7, it can be concluded that for Flexisource Co-60 seed the difference at short (less than 0.5 cm) and large distances (more than 8 cm) from the source was between 1 and 6%; however, at distances between 0.5 to 8 cm, there was a considerable agreement between the two diagrams. Thus, for all three seeds, although there was no significant difference in the parameter $g(r)$, the observable differences can be attributed to small differences in the dimensions and structure of the source, the spectra used, the inequality of electrons and photons cutoff energy, etc.

According to the diagrams of the anisotropy function for 6711 I-125 seed (Figs. 8 to 13), it can be concluded that elevating the angular distance from the source provides a higher agreement between the present study and the Dolan's study. This indicated that the impact of the factors causing the difference in the absorbed dose between the present study results and Dolan's publication (cited in the comparative section of the radial dose function) became lesser with increasing angular distance. On the other hand, as shown in Figs. 14 to 17, examining the parameter $F(r, \theta)$ on the Micro Selectron mHDR-v2r Ir-192 seed showed that except in rare cases (where the difference in values with López study is exceeds 1%), the differences in the majority of conditions were below 1%. Finally, by comparing the parameter $F(r, \theta)$ for the Flexisource Co-60 seed to the present study and Vijande's article (as shown in Figs. 18 to 23), it can be inferred that the differences are completely acceptable for most angles at different distances (differences below 1%) except in some places at low angles (with differences 1% to 2%). Therefore, in the case of Co-60 seed, it was also observed that the amount of difference decreases with increasing angular distance from the source.

## 5 Conclusions

Experimental challenges can lead to inaccurate determination of the dosimetric parameters necessary to accurately compute the dose for brachytherapy treatments. The Monte Carlo MCNP5 code was utilized for the 6711 I-125, MicroSelectron mHDR-v2r Ir-192, and Flexisource Co-60 source models in order to correctly compute their dosimetric parameters. The dose rate constant for the three I-125, Ir-192, and Co-60 seeds were 0.949, 1.1087, and 1.15 cGy.h$^{-1}$/cGy.m$^2$.h$^{-1}$ respectively, which were inconsistent with the Dolan's article. Furthermore, a comparison of the $g(r)$ and $F(r, \theta)$ parameters for the three sources with the data of the mentioned studies demonstrated an acceptable consistency, so that these datasets can be used as input in the treatment planning systems and to validate its calculations.

## Acknowledgment

This research was supported by grant No. [14259] from the School of Medicine, Iran University of Medical Sciences (IUMS).

## Conflict of Interest

The authors declare no potential conflict of interest regarding the publication of this work.



## References

Alizadeh, M., Ghorbani, M., Haghparast, A., et al. (2015). A Monte Carlo study on dose distribution evaluation of Flexisource Ir brachytherapy source. *Reports of Practical Oncology and Radiotherapy*, 20(3):204–209.

Cross, W. G., Soares, C. G., Vynckier, S., et al. (2003). Dosimetry of beta rays and low-energy photons for brachytherapy with sealed sources, ICRU Report 72.

DeMarco, J., Solberg, T., and Smathers, J. B. (1998). A CT-based Monte Carlo simulation tool for dosimetry planning and analysis. *Medical Physics*, 25(1):1–11.

Dolan, J., Li, Z., and Williamson, J. F. (2006). Monte Carlo and experimental dosimetry of an brachytherapy seed. *Medical Physics*, 33(12):4675–4684.

Huh, H., Kim, W., Loh, J. J., et al. (2007). Rectum dose analysis employing a multi-purpose brachytherapy phantom. *Japanese Journal of Clinical Oncology*, 37(5):391–398.

IAEA (2000). Absorbed dose determination in external beam radiotherapy: An international code of practice for dosimetry based on standards of absorbed dose to water, IAEA technical reports series No. 398, International Atomic Energy Agency.

Kacperek, A. (2000). Clinical proton dosimetry Part I: Beam production, beam delivery and measurement of absorbed dose (ICRU Report 59).

López, J. A., Donaire, J. T., and Alcalde, R. G. (2011). Monte Carlo dosimetry of the most commonly used Ir-192 high dose rate brachytherapy sources. *Rev Fis Med*, 12(3):159–168.

MCNP5 (2008). MCNP5/MCNPX-exe package, Monte Carlo N-particle extended. Technical report, Los Alamos National Laboratory report.

Mostaar, A., Alahverdi, M., and Shahriari, M. (2003). Application of MCNP4C Monte Carlo code in radiation dosimetry in heterogeneous phantom.

Nath, R. (1995). Response to "Comments onDosimetry of interstitial brachytherapy sources: Recommendations of the AAPM Radiation Therapy Committee Task Group No. 43"' [Med. Phys. 22, 209-234 (1995)]. *Medical Physics*, 22(8):1351.

Rivard, M. J. (2009). Monte Carlo radiation dose simulations and dosimetric comparison of the model 6711 and 9011 brachytherapy sources. *Medical Physics*, 36(2):486–491.

Rivard, M. J., Coursey, B. M., DeWerd, L. A., et al. (2004). Update of AAPM Task Group No. 43 Report: A revised AAPM protocol for brachytherapy dose calculations. *Medical Physics*, 31(3):633–674.

Sadeghi, M. and Hosseini, S. H. (2010). Study of the IsoAid ADVANTAGE 125I brachytherapy source dosimetric parameters using Monte Carlo simulation. *Applied Radiation and Isotopes*, 68(1):211–213.

Sadeghi, M., Hosseini, S. H., and Raisali, G. (2008a). Experimental measurements and Monte Carlo calculations of dosimetric parameters of the IRA1-Pd-103 brachytherapy source. *Applied Radiation and Isotopes*, 66(10):1431–1437.

Sadeghi, M., Raisali, G., Hosseini, S. H., et al. (2008b). Monte Carlo calculations and experimental measurements of dosimetric parameters of the brachytherapy source. *Medical Physics*, 35(4):1288–1294.

Saidi, P., Sadeghi, M., Shirazi, A., et al. (2010). Monte Carlo calculation of dosimetry parameters for the IR08-brachytherapy source. *Medical Physics*, 37(6Part1):2509–2515.

Urie, M., Goitein, M., and Wagner, M. (1984). Compensating for heterogeneities in proton radiation therapy. *Physics in Medicine & Biology*, 29(5):553.

Vijande, J., Granero, D., Perez-Calatayud, J., et al. (2012). Monte Carlo dosimetric study of the Flexisource Co-60 high dose rate source. *Journal of Contemporary Brachytherapy*, 4(1):34–44.

Williamson, J., Coursey, B. M., DeWerd, L. A., et al. (1998). Dosimetric prerequisites for routine clinical use of new low energy photon interstitial brachytherapy sources. Recommendations of the American Association of Physicists in Medicine Radiation Therapy Committee. Ad Hoc Subcommittee of the Radiation Therapy Committee. *Medical Physics*, 25(12):2269–2270.

RPE | Radiation Physics & Engineering
An International Peer-Reviewed Journal
Published by K.N. Toosi University of Technology
http://rpe.kntu.ac.ir
Research Article

Radiation Physics and Engineering 2022; 3(4):17–21
https://doi.org/10.22034/rpe.2022.335909.1067

# Design of a two-dimensional pseudo coincidence Compton suppressor system for neutron activation analysis

Ali Biganeh, Banin Shakeri Jooybari*

*Physics & Accelerators Research School, Nuclear Science and Technology Research Institute, P.O. Box 14395-836, Tehran, Iran*

## HIGHLIGHTS

- A new Compton suppressor system is designed using two face-to-face HPGe detectors.
- The algorithm for the identification of pseudo coincidence events from list data is presented.
- The double coincidence events are explained and removed using trigger hold-off technique.
- The developed system provides low-background high-resolution spectrometer for NAA.

## ABSTRACT

Compton scattering events are the main source of error on the peak counting during the Neutron Activation Analysis (NAA). The Compton suppressor system in instrumental NAA reduces the detection limit of the technique and leads to a data with a higher degree of precision. In this paper, a two-dimensional coincidence Compton suppressor system is presented for the NAA technique. The system is established based on a CAEN digitizer which directly records the pre-amplifier output signals of the two HPGe detectors. The recorded events in the list mode file are analyzed offline by a Matlab code and the correlated photopeak events are realized. The performance of the system for Compton suppression is tested by measuring the gamma lines of Ba-133 and Cs-137 standard sources. The results show that the presented technique provides the peak to Compton ratio up to $10^4$ and can be an alternative for conventional Compton suppressor systems.

## KEYWORDS

Compton suppressor
Neutron Activation Analysis
List mode
Digitizer

## HISTORY

Received: 5 April 2022
Revised: 6 June 2022
Accepted: 24 June 2022
Published: Autumn 2022

## 1 Introduction

Instrumental Neutron Activation Analysis is a well-established non-destructive technique for the determination of elements and their concentration in the bulk of the samples (Munita et al., 2019). The technique is based on the activation by neutron using neutron emitter radioisotope sources or research reactor facilities. After activation via $(n, \gamma)$ reaction, the gamma-ray spectroscopy of the resulting compound nucleus performs using a high-resolution detector to determine the yield of gamma lines in the spectrum. Each gamma line is a specific signature of the elements and its yield determines the concentration of an element in the content. The quality of gamma-ray spectroscopy has a significant effect on the accuracy of the results. The conventional gamma-spectroscopy system in this method includes an HPGe detector, power supply, spectroscopy amplifier, and a computer equipped with suitable software for recording and data analysis. Since the investigated samples (soil, plant, milk, and alloys) contain a large number of elements, their related gamma spectrum includes many (10 to 100) peaks (Landsberger et al., 2002). The most important source of error during the analysis is the background spectrum caused by Compton scattering and its overlap with the other gamma lines. The Compton background leads to the disappearance of many peaks or even if observed, due to the predominance of the Compton, the value of the area under the peak is inaccurate. The Compton background in the recorded spectrum reduces the sensitivity and detection limits for the determination of some elements such as U, As, Th, and Ca. So the result of the analysis of that particulate elements will be reported with great inaccuracy in the presence of Compton events on the spectrum. To overcome the mentioned problem, in a typical gamma-ray spectroscopy system used for NAA, a Compton suppression system is used to increase the peak to Compton ratio (Stover and Lamaze, 2005). A perusal of the literature reveals that the use of the Compton suppression system improves the detection limit for As, Ca, Cd, Cr, Fe, Hg,

*Corresponding author: bshakeri@aeoi.org.ir

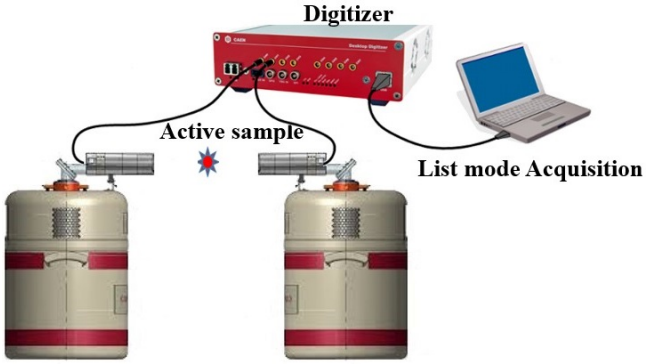


**Figure 1:** The schematic of the designed Pseudo coincidence Compton suppressor system.

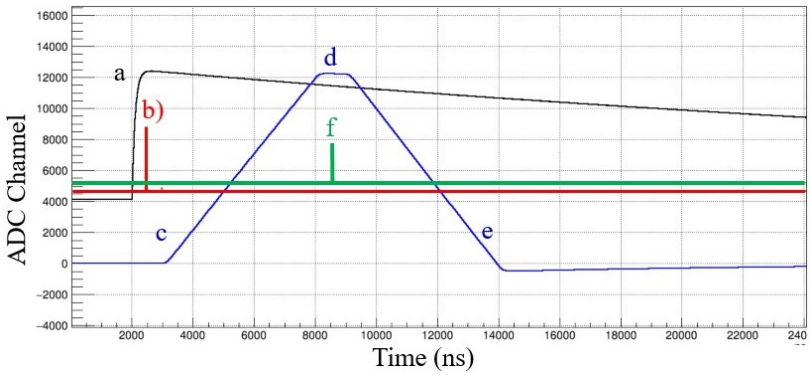


**Figure 2:** The signal inspector view: a) preamplifier signal, b) trigger, c) rise time of the trapezoidal energy filter, d) flat-top time, e) decay time of trapezoidal filter, f) Time tag.

K, Rb, Zn, Th, and U elements in geological, environmental, biological, archeological, and agricultural samples (dos Santos et al., 2012; Mauerhofer et al., 1996).

A typical Compton suppressor system includes a central HPGe detector surrounded by either NaI (Tl) or BGO detectors. The Compton scattering events will be detected by both detectors and the photo peaks will be detected by the HPGe detector. The acquisition system measures the gamma-rays in anti-coincidence mode. The mentioned Compton suppressor systems are expensive (about 150 k$) and are not easy to access. In this paper, a 2D pseudo coincidence Compton suppressor system is designed using two conventional HPGe detectors.

## 2 Materials and methods

The presented spectrometer at Nuclear Science and Technology Institute (NSTRI) is established based on a 14-bit CAEN waveform digitizer (CAEN DT5730) that samples directly from the preamplifier output of the two face-to-face HPGe detectors (ORTEC-GEM 20200, Canberra3001c). Figure 1 shows the schematic of the designed system. In this configuration, all the nuclear electronic modules are omitted and the system is loaded with firmware. Figure 2 shows the signal inspector view of the digitizer (Caen, 2022). The algorithm that transforms the sampled raw waveforms (Fig. 2-a) to a trapezoidal signal is based on the Jordanov energy filter and is called Pulse Height Analyzer (PHA) (Jordanov and Knoll, 1994). The trapezoid filter plays the role of a Gaussian filter of shaping amplifier in analog nuclear electronics. The advantages of the trapezoidal filter compared to Gaussian filter for high-resolution low-level background gamma-ray spectroscopy have been clarified by Jordanov et al.(Jordanov et al., 1994). The height of the trapezoid flat-top (Fig. 2-d) at the time tag (Fig. 2-f) is proportional to the energy of radiation. The procedure for optimum selection of energy filter parameters (rise time, flat-top time, decay time, baseline mean, etc.) can be found in our previous paper (Biganeh et al., 2019). After the correct configuration of the setting for each channel of the digitizer, the MC2 software records the energy and the timestamp of the all detected events in two detectors and stores them in a text file (Caen, 2018). The procedure for recognizing the pseudo coincidence events is described in the next section.

## 3 Experimental Details

To test the performance of the system, the detected gamma-rays of Ba-133 (276.4, 302.9, 356, 383.8 keV) and Cs-137 (662 keV) in the two detectors are recorded in a list file (a file contains the energy and time of each event). The experiment lasted 4 hours to record enough photopeak events on the list. The size of the list file is 2 GB for each channel of the digitizer. The algorithm for the identification of pseudo coincidence events and conversion of list-mode data to the 2D spectrum is shown in Fig. 3.

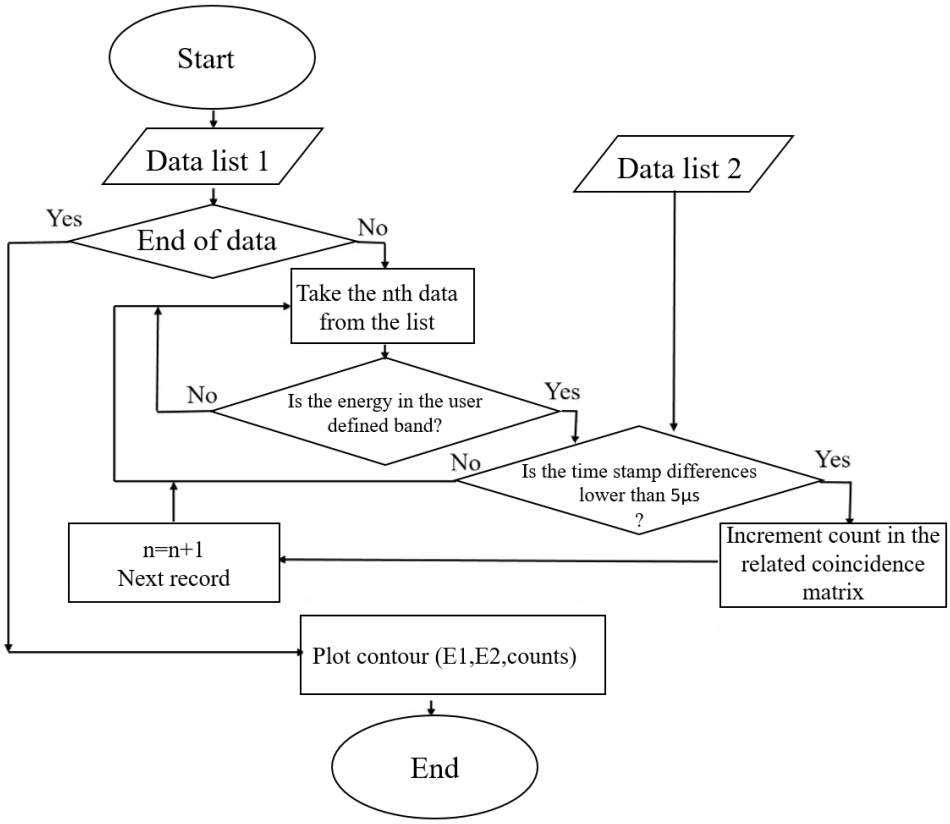


**Figure 3:** The algorithm for conversion of list-mode data to the 2D spectrum.

Using this algorithm, the offline analysis of the list mode data is done to extract the pseudo coincidence correlated counts.

The problem that appears during data analysis using the mentioned algorithm is the record of double coincidence events on the list data due to the large coincidence time window in pseudo coincidence mode. Figure 4 well describes the condition where the double coincidence occurs. As shown in Fig. 4, in the case of coincidence between channels #1 and #2, for each valid trigger, a trigger validation gate propagates with a bandwidth of TST. In the case of double coincidence, two events of channel #1 (shown as a and b) are in coincidence with a single event (shown as c) of the other channel. So, when the trigger validation gates of the two channels overlap each other, the first overlap enables the first signal of channels #1 and #2 and the second overlap records the signal of channel #1 but there is no valid signal in channel #2 (case. 1 in Fig. 4). During the data acquisition, the double coincidence event is an interrupting factor in recognizing correlated events. To avoid this phenomenon, the trigger hold-off parameter of the energy filter is set greater than twice the pseudo coincidence time window. The trigger hold-off prevents the re-triggering of the signal at channel 1 and the recorded events in list mode one by one correlate with one another (case. 2 in Fig. 4).

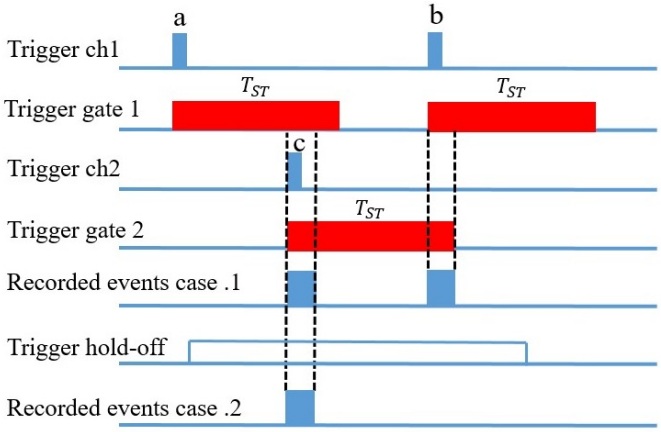


**Figure 4:** The description of the double coincidence event in channel #1.

## 4 Results and discussion

In the offline analysis of the list-mode data, the optimum value of 5s is selected for the pseudo coincidence time window to obtain the maximum peak to Compton ratio and to efficiently detect the chance coincidence gamma-rays of Ba-133 (0.11 $\mu$Ci) and Cs-137 (0.08 $\mu$Ci). The pseudo coincidence time window just confirms that the detected events are virtually correlated and allows the record of events in a matrix. However, the issue that needs to be addressed is that the efficiency of the coincidence acquisition

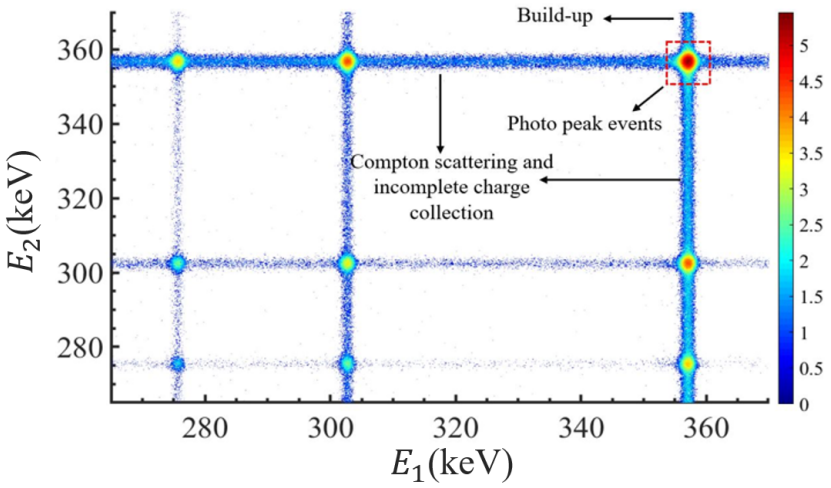


**Figure 5:** The 2D pseudo coincidence spectrum of Ba-133 radioisotope. The gamma-region of 256, 302, and 356 keV of Ba-133.

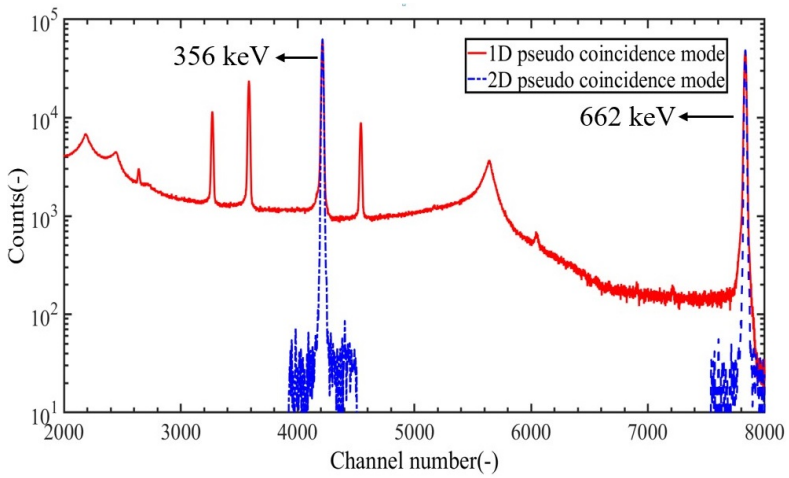


**Figure 6:** The projection of the 2D spectrum with a bandwidth of 10 keV is also shown.

system must be constant for NAA samples with different activities for the preset pseudo coincidence time window. The expected activities of a sample in NAA are as follows:

- 0.01 to 0.1 $\mu$Ci for long half-life elements.
- 1 to several $\mu$Ci for medium half-life elements.
- 10-20 $\mu$Ci for short half-life elements.

We consider the upper case and assume that the activity is 20 $\mu$Ci. This activity is equivalent to $7.4 \times 10^5$ d.s$^{-1}$ ($7.4 \times 10^{-1}$ d.$\mu$s$^{-1}$). So, the coincidence time window (5 $\mu$s) is large enough to record the events without any loss if seen by a detector.

Assume that $E_1$ and $E_2$ are the recorded energy by detectors #1 and #2, respectively. A $5500 \times 5500$ matrix array of $E_1$ and $E_2$ events is built-up. Figure 5 shows the 2D pseudo coincidence spectrum of the gamma-rays. Due to limitations in the RAM of our computer, we plot the data in the 270 to 370 keV region. The circles shown on the matrix diameter represent the background-free photopeak events. This region carries the most valuable information about the NAA experiment. The ridges parallel to the axis are Compton scattered (low energy sides) or pile-up events (high energy sides). To obtain the photopeak events a diagonal cut of the matrix with a bandwidth of 10 keV is selected. Figure 6 shows the projection of the 2D spectrum to the conventional 1D spectrum for gamma lines of 356 and 662 keV. As shown in Fig. 6, by separation of unwanted events such as Compton scattering, background, and pile-up, the peak to Compton ratio increased up to $10^4$ in the 2D pseudo coincidence mode. Moreover, the energy resolution of the 2D spectrometer (RT) can be predicted by the resolution of each HPGe detector using Eq. (1) (Čížek et al., 2010):

$$R_T = \frac{1}{2}\sqrt{R_1 + R_2} \tag{1}$$

## 5 Conclusions

In the past decade, many efforts have been devoted to using Compton suppression systems for NAA. These systems are often very expensive and include complex nuclear elec-

tronics. In this paper, we switched from analog to digital gamma-ray spectroscopy to design a Compton suppressor system using conventional HPGe detectors. The results of our experiment confirm that the 2D gamma-ray spectroscopy using a list mode file can increase the peak to Compton ratio up to $10^4$ and improves the spectrometer energy resolution. Moreover, due to the use of Pseudo coincidence data acquisition, no lead shielding is needed in the presented technique. Although significant improvements have been achieved using the 2D Compton suppresser system, this technique needs a long time of data acquisition (4 hours) to obtain enough data of photopeak events to project the 2D spectrum to a conventional histogram. Further to this work, we are going to initiate a series of NAA experiments using the presented technique to investigate the possible improvement of the detection limit in the NAA technique.

## Conflict of Interest

The authors declare no potential conflict of interest regarding the publication of this work.

## Open Access



## References

Biganeh, A., Kakuee, O., Rafi-Kheiri, H., et al. (2019). Development of a 2D digital coincidence Doppler broadening spectrometer. *Journal of Instrumentation*, 14(02):P02017.

Caen (2018). Caen Electronic Instrumentation, MC2 analyzer user manual, v. 3. Technical report.

Caen (2022). Caen Electronic Instrumentation, compass multi-parameter DAQ software for physics applications, revision 2.0.1, February $15^{th}$ 2022. Technical report.

Čížek, J., Vlček, M., and Procházka, I. (2010). Digital spectrometer for coincidence measurement of Doppler broadening of positron annihilation radiation. *Nuclear Instruments and Methods in Physics Research Section A: Accelerators, Spectrometers, Detectors and Associated Equipment*, 623(3):982–994.

dos Santos, L., Bacchi, M., De Nadai Fernandes, E., et al. (2012). Performance of Compton suppression system (CSS) and applicability in food matrices. *Journal of Radioanalytical and Nuclear Chemistry*, 291(1):179–185.

Jordanov, V. T. and Knoll, G. F. (1994). Digital synthesis of pulse shapes in real time for high resolution radiation spectroscopy. *Nuclear Instruments and Methods in Physics Research Section A: Accelerators, Spectrometers, Detectors and Associated Equipment*, 345(2):337–345.

Jordanov, V. T., Knoll, G. F., Huber, A. C., et al. (1994). Digital techniques for real-time pulse shaping in radiation measurements. *Nuclear Instruments and Methods in Physics Research Section A: Accelerators, Spectrometers, Detectors and Associated Equipment*, 353(1-3):261–264.

Landsberger, S., Iskander, F., Niset, M., et al. (2002). Compton suppression gamma ray spectrometry. Technical report.

Mauerhofer, E., Tharun, U., Denschlag, H., et al. (1996). A compton suppression spectrometer for neutron activation analysis. *Nuclear Instruments and Methods in Physics Research Section A: Accelerators, Spectrometers, Detectors and Associated Equipment*, 371(3):465–471.

Munita, C. S., Glascock, M. D., and Hazenfratz, R. (2019). Neutron activation analysis: an overview. *Recent Advances in Analytical Techniques*, 3:179–227.

Stover, T. and Lamaze, G. (2005). Compton suppression for neutron activation analysis applications at the National Institute of Standards and Technology (NIST). *Nuclear Instruments and Methods in Physics Research Section B: Beam Interactions with Materials and Atoms*, 241(1-4):223–227.

RPE | Radiation Physics & Engineering
An International Peer-Reviewed Journal
Published by K.N. Toosi University of Technology
http://rpe.kntu.ac.ir
Research Article

Radiation Physics and Engineering 2022; 3(4):23–29
https://doi.org/10.22034/rpe.2022.337040.1073

# Dynamic behavior analysis of different pressurizer types on a high-pressure test facility

Abolfazl Shoghi*, Seyed Ali Hosseini, Amir Saeed Shirani, Mahdi Zangian
*Faculty of Engineering, Shahid Beheshti University, Tehran, Iran*

## HIGHLIGHTS

- The dynamic behavior of Steam, Gas-Steam, and Gas PRZ is evaluated in the WHPCHF facility.
- The peak pressure of different types of PRZs is compared during the same scenario.
- The Gas PRZ has the highest peak pressure due to the lack of non-condensable gas condensation.

## ABSTRACT

The pressurizer is a key equipment to ensure the safe operation of pressurized water reactor by maintaining the reactor coolant system pressure within allowed tolerances. Various pressure control systems (Pressurizer) are adopted in industrial applications to satisfy their characteristics. In accordance with the purpose of using nuclear facilities, steam, gas-steam, and gas pressurizer (PRZ) have been used. In nuclear industry, the dynamic behavior of each PRZ is different. Peak pressure is one of the important parameters in choosing the type of PRZ. This study has been evaluated for the University of Wisconsin High-Pressure Critical Heat Flux (WHPCHF) facility as the base loop. Three PRZs are connected to the WHPCHF loop to evaluate their performance during the in-surge scenario. The Peak pressure of the three PRZs is evaluated during transients. The results showed that the use of the Non-condensable Gas (NCG) increases the peak pressure due to the lack of NCG condensation during transient conditions. The use of gas PRZ makes it possible to change the pressure quickly. Also, the pure gas PRZ has the highest peak pressure but has straightforward control logic. The gas PRZ is the best choice for small reactors and high-pressure test facilities.

## KEYWORDS

Pressurizer
Dynamic behavior
Peak pressure
Control logic
Test facilities

## HISTORY

Received: 10 April 2022
Revised: 29 June 2022
Accepted: 2 July 2022
Published: Autumn 2022

## 1 Introduction

The pressure control system (pressurizer) plays a key role in pressurized water processes. Pressurizer (PRZ) is one of the most important equipments used in the nuclear industry. The purpose of the pressurizer is to keep the pressure constant within the operational limit. On the other hand, the main task of the PRZ system is to control the pressure on the desired limit during transients causing temperature and pressure changes in the system. All of these transients in the main loop affect the PRZ, regulating the pressure and the level (Shoghi et al., 2021). The type of PRZ is selected based on the purpose of the industrial process. PRZs in the nuclear industry are classified into three groups, which include gas, gas-steam, and steam PRZ. Gas PRZs are a group of PRZs used in test facilities, research reactors and, even SMRs. The main part of the gas PRZ is the Non-Condensable Gas (NCG) zone. The presence of the NCG increases the peak pressure due to the lack of NCG condensation during transient and accident conditions. Thus, in the small volume ratio of steam inside the PRZ, it seems that adding gas is not appropriate. Because it increases the peak pressure further and the pressure increases rapidly even during the small transients. Of course, from another perspective, the work of the spray is reduced by adding NCG. Also, the pure gas PRZ has the highest peak pressure but has easy control logic. In other words, the use of gas PRZ makes it possible to change the pressure quickly. The gas PRZ is the best choice for propulsion reactors and high-pressure test facilities. Also, the gas PRZ can be used passively (Shoghi et al., 2021).

Steam PRZs is the most common type of PRZs in the nuclear industry used in most power reactors. On the other hand, The study on the steamgas pressurizer has been rarely done compared to the steam pressur-

*Corresponding author: ab.shoghi@mail.sbu.ac.ir

izer because there is only a small number of the nuclear reactors using steamgas pressurizer (Kim et al., 2006). The gas PRZ is very different from the steam PRZ and has been less widely researched than other PRZs (Shoghi et al., 2021). Studies have been performed on the mathematical modeling of PRZs. Mathematical modeling of PRZs well illustrates their dynamic behavior during transient and accident conditions. Pini et al. (Pini et al., 2018) mathematically modeled the steam PRZ for a Pressurized Water Reactor (PWR) and developed a control-oriented model based on the non-equilibrium equations. Zhong et al. (Zhong et al., 2019) used an improved non-equilibrium multi-region model for the accurate prediction of pressure in the steam pressurizer of PWR under transient conditions. Wang et al. (Wang et al., 2019) developed a nonequilibrium three-region pressurizer model for the steam PRZ of PWR. The given model was linearized to introduce the transfer function models of the pressurizer during in-surge and out-surge transients for the controller design of a small pressurized water reactor pressurizer. Moghanaki and Rahgoshay (Moghanaki and Rahgoshay, 2014) used two-region and four-region thermodynamic models for the simulation of a typical PWR pressurizer and benchmarked the calculated results with RELAP5/Mod3 code findings. Baghban et al. (Baghban et al., 2016) employed a simple numerical model based on the non-equilibrium, multi-region model to simulate the pressurizer behavior during transient conditions. Cheng et al. (Cheng et al., 2009) developed a pressurizer model with TRACE code version 5.0 and performed The benchmark of the pressurizer model by comparing the simulation results with those from the tests at the Maanshan nuclear power plant. Hosseini et al. (Hosseini et al., 2020) modeled the thermal-hydraulic behavior of the PRZ by RELAP5 thermal-hydraulic code and coupled the RELAP5 code and MATLAB software to provide a new platform for designing and implementing various intelligent and advanced controllers for PRZ pressure and level in RELAP5 code. Lotfi et al. (Lotfi et al., 2020) simulated the PRZ of VVER-1000 with RELAP5 code. Farman et al. (Farman et al., 2017) performed the study and analysis of the dynamic transient behavior of the pressurizer of PWR. de Oliveira et al. (2013) developed a pressurizer model based on artificial neural networks (ANNs) and developed fuzzy controllers for the PWR pressurizer modeled by the ANN and compare their performance with conventional ones. In addition, many researchers have studied the mathematical simulation for dynamic characteristics of the steam PRZ (Redfield et al., 1968; Baron, 1973; Abdallah et al., 1982; Baggoura and Martin, 1983; Beak, 1986; Wu et al., 2010). The steam-gas PRZ in integrated small reactors experiences very complicated thermal-hydraulic phenomena especially; the condensation heat transfer with NCG under natural convection is an important factor to evaluate the PRZ behavior. Hassan and Banerjee (Hassan and Banerjee, 1996) used the relap5/mod3 thermal-hydraulic code to study the ability of the code to predict Condensation phenomena in the presence of non-condensable gases. Kim et al. (Kim et al., 2008) numerically analyzed gas-steam PRZ's transitions. Wu et al. (Wu et al., 2013) studied transient characteristics of the gas-steam typed pressurizer using the Relap5 code. Lee and Park (Lee and Park, 2013) have researched a thermal-hydraulic system code for transient analysis of a fully-passive integral PWR and presented equations for a gas-steam PRZ. Yoder et al. (Yoder Jr et al., 2014) evaluated the Liquid-Fluoride-Salt test loop that is used an accumulator tank supported by argon gas to control the loop pressure. O'Brien et al. (O'Brien et al., 2017) analyzed the high temperature and pressure test facility that is used an accumulator tank to regulate pressure with supporting nitrogen gas. Xi et al. (Xi et al., 2015) developed mathematical models to study the thermal-hydraulic characteristics of the passive residual heat removal system under ocean conditions. Corradini and Wu (Corradini and Wu, 2015) evaluated the University of Wisconsin High-Pressure Critical Heat Flux (WHPCHF) that is connected to cylinders containing argon gas. Shoghi et al. (Shoghi et al., 2021) first developed mathematical modeling of gas PRZ. The results of the mathematical model are compared with the results of HYSYS. Similar mathematical equations will extend in this paper to simulate the gas PRZ.

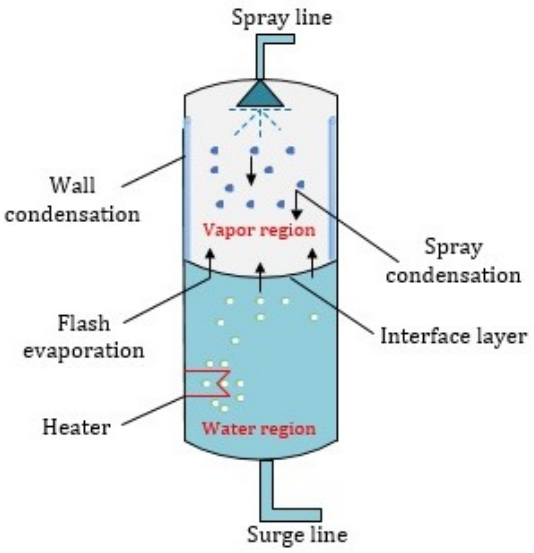


**Figure 1:** The steam PRZ schematic.

## 2 Pressurizer system in industrial process

PRZs in the nuclear industry are classified into three groups. Steam PRZ is the most common type of PRZ in the nuclear industry. The steam PRZ operates in equilibrium with a mixture of water and steam. As shown in Fig. 1, the Steam PRZ utilizes two main strategies to control the primary loop pressure within the specified limits. The first strategy is to condense the steam through the cold-water spray to decrease the pressure, and the second strategy is to heat the water with the PRZ electrical heaters to increase the pressure. As shown in Fig. 2, the steam-gas PRZ has been composed based on the non-equilibrium two-region. The steam-gas PRZ uses a single volume consisting of two semi-independent regions, each with special

thermodynamic conditions. Another presumption about steam-gas PRZ is that steam and non-condensable gas are combined in the gas region, and mass and energy are transferred between two regions at the interface area. This type of PRZs is also emphasized in a new generation of SMRs, such as the SMART Korean design reactor. In the steam-gas PRZ, the non-condensable gases are applied as controlling actuator mechanisms instead of electrical heaters and sprays (compared with steam PRZ), including the nitrogen and argon, in the steam-gas mixture area.

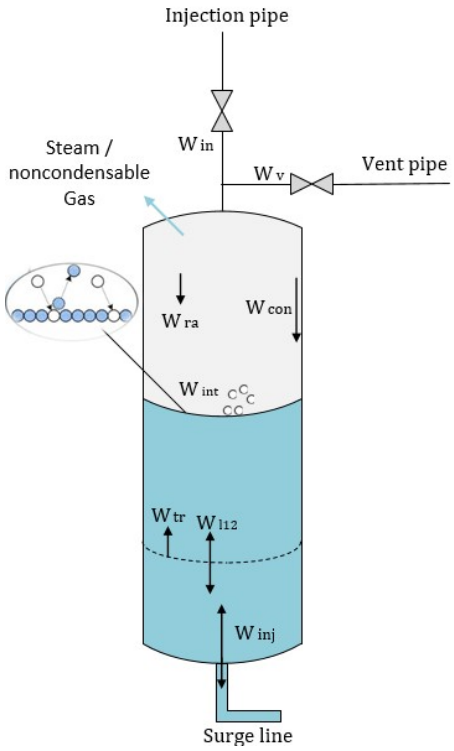


**Figure 2:** The steam-gas PRZ schematic.

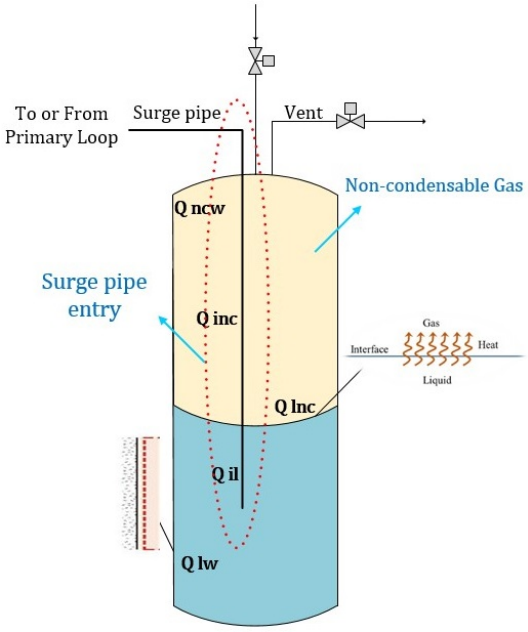


**Figure 3:** The gas PRZ schematic.

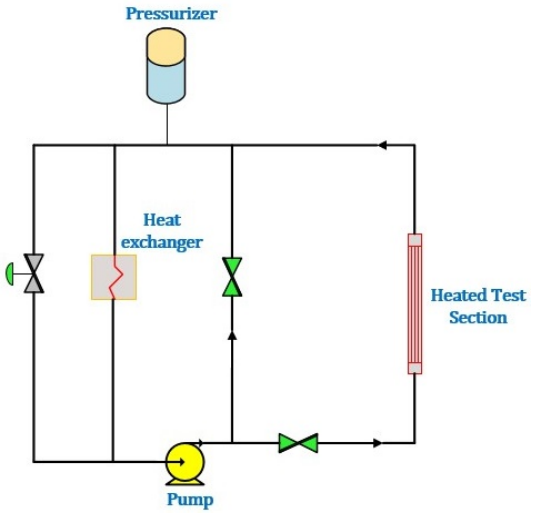


**Figure 4:** Overview of the main Wisconsin-Madison facility.

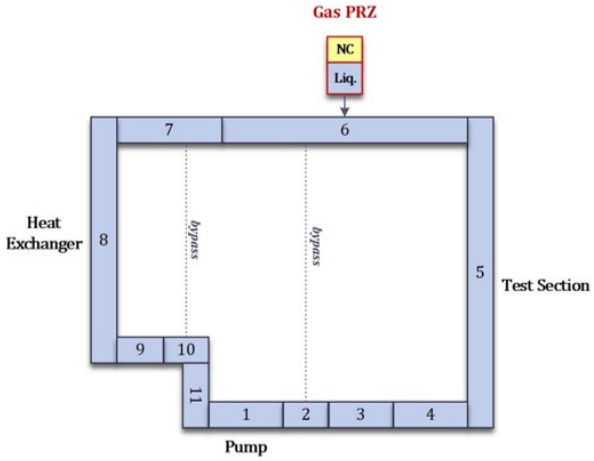


**Figure 5:** Nodalization of control volumes in the WHPCHF loop.

The gas PRZ (Fig. 3) is another type of PRZ which is controlled by a non-condensable gas that does not mix with the steam. The performance and operation of gas PRZs are different, and less research has been done than other types of PRZs. Therefore, the PRZ is separated into two water and gas regions with different phases and enthalpies of the liquid. In addition, the gas PRZ can be used in the high flux research reactor and SMRs. The working principles of gas PRZs are different from steam PRZs. The gas PRZ separates into two parts, liquid, and non-condensable gas, according to phases and enthalpies of the fluid.

## 3 Simulated model in HYSYS

Aspen HYSYS is one of the unique tools for chemical processes that are used in various manufacturing processes. Aspen HYSYS is capable of performing many engineering calculations, including mass balance, energy balance, heat transfer, Pressure drops, liquid-vapor balance, mass transfer, chemical kinetics, and more. This program is

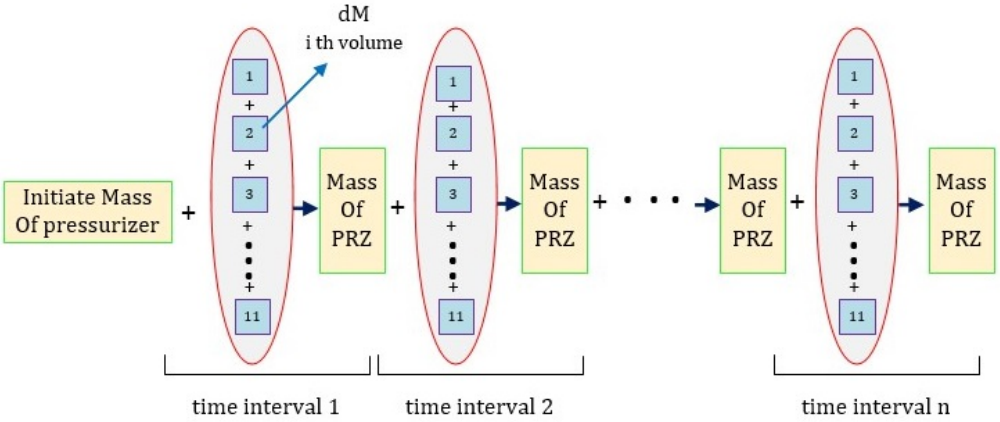


**Figure 6:** General schematic of the model's performance.

commonly used for steady-state and dynamic simulation, process design, and optimization.

### *3.1 WHPCHF facility*

The University of Wisconsin High-Pressure Critical Heat Flux (WHPCHF) facility is specifically designed to obtain CHF data under unique operating conditions. The WHPCHF facility consists of various equipment (Fig. 4); the WHPCHF facility's key equipment is the high-pressure pump, high-temperature test section, heat exchanger, gas PRZ, argon cylinders, and the air chiller. All of the components are integrated with the Aspen HYSYS environment, and the primary loop of WHPCHF is divided into 11 control volumes, as shown in Fig. 5. In each time interval, the total mass changes in the interval are obtained by adding all of the mass changes in control volumes, as shown in Fig. 6.

All three PRZs are simulated in Aspen HYSYS. Each is operated in a similar scenario. It should be noted that the geometry of all three PRZs is similar. the main characteristics of presented PRZs are presented in Table 1.

**Table 1:** Main characteristics of the presented PRZ.

| Parameter | Unit | Value |
|---|---|---|
| PRZ Volume | $m^3$ | $4.35 \times 10^{-2}$ |
| PRZ height | m | 2.384 |
| Water Region Volume | $m^3$ | $2.376 \times 10^{-2}$ |
| PRZ Cross-sectional area | $m^2$ | $1.824 \times 10^{-2}$ |

### *3.2 Simulated three PRZs (Steam, Gas-Steam, and Gas PRZ) description with Aspen HYSYS*

The Aspen HYSYS software and RELAP5 code are the best options for thermal-hydraulic modeling of PRZ. It should be noted that the RELA5 code has imperfections to model the gas PRZs. In other words, the RELAP5 cannot model the pure NCG region. Thus, the RELAP5 just models the volume with a mixture of water/steam/NCG when the volume of NCG has a low percentage. Therefore, in this study, Aspen HYSYS software is selected to simulate gas PRZ. Aspen HYSYS is one of the unique tools for industrial processes that are used in various manufacturing processes.

It should be noted that the gas PRZ is not defined in the list of Aspen HYSYS equipment. Therefore, a separator has been used to create the geometry of the gas PRZ. Separator boundary conditions are selected according to the WHPCHF gas PRZ boundary conditions. The nodalization of the separator and its boundary conditions are presented in Fig. 7. There are two regions for the steam PRZ (steam and water region). There is steam in the upper part of the PRZ and water (liquid) in the lower part (Fig. 1). Also, there are two regions in the Gas-Steam PRZ (mixed and water regions). In the mixed region, there is a mixture of NCG and steam (Fig. 2). In this study, three PRZs are connected to the WHPCHF loop to evaluate their performance during the same scenario. Because the top region of each PRZ is different, their behavior will also be different (Table 2).

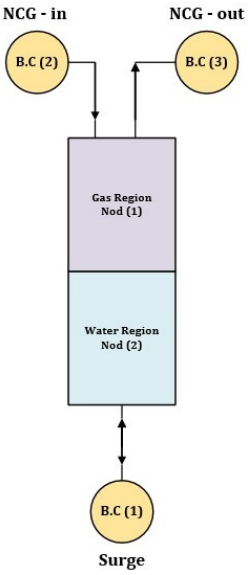


**Figure 7:** Separator nodalization and boundary conditions.

**Table 2:** Contents of each PRZ.

| PRZ type | Bottom region | Upper region |
|---|---|---|
| Steam PRZ | liquid | Vapor |
| Gas-Steam PRZ | liquid | Vapor-NCG |
| Gas PRZ | liquid | NCG |

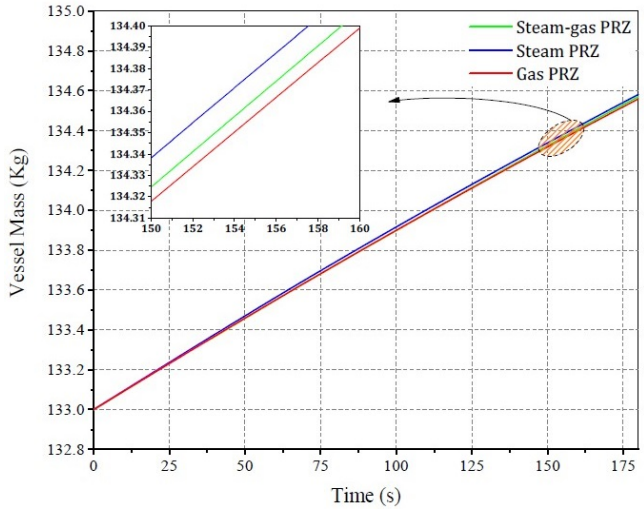


**Figure 8:** Mass Changes during In-Surge Scenario.

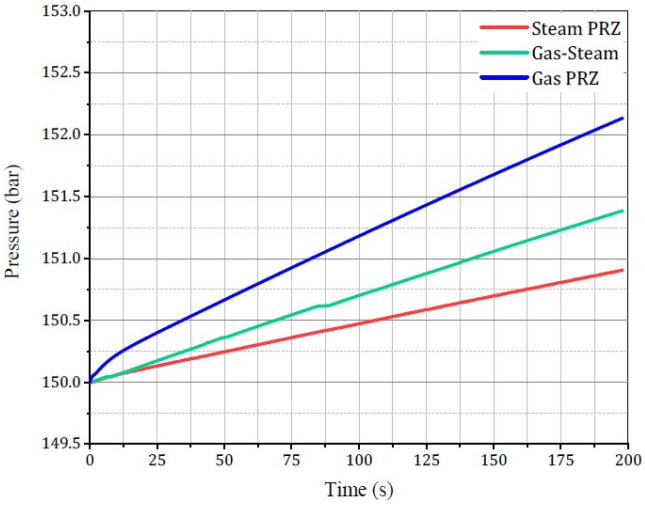


**Figure 9:** Pressure Change inside the PRZs.

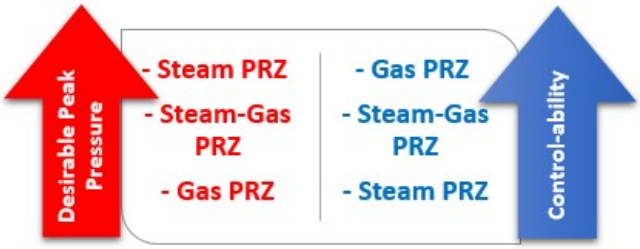


**Figure 10:** The PRZs comparison is based on their peak pressure and control-ability in transients.

### *3.3 In-surge scenario*

A scenario has been implemented to test the performance of each PRZ. During the In-surge scenario, the chiller in the secondary loop removes less heat from the loop and, the heat removed from the primary loop decreases. Therefore, the temperature in the primary loop increases over time. In addition to increasing the temperature, the specific volume inside the main loop increases as a function of specific enthalpy and pressure (Eq. (1)). During this scenario, by increasing the pressure, some water from the primary loop has entered the PRZ.

$$v = f(P, h) \tag{1}$$

In the case of loop malfunction, the specific volume changes in each control volume. Therefore, it changes the mass in each of the control volumes. The mass changes are collected in all control volumes and applied to the PRZ at each time interval (Fig. 6). This scenario is applied to all three PRZs.

## 4 Results and discussion

During the in-surge scenario, the temperature in the primary loop increases over time. In addition to increasing the temperature, the specific volume inside the main loop increases. During this scenario, by increasing the pressure, some water from the primary loop has entered the PRZ. The comparison of the mass changes inside the different types of PRZs is presented (Fig. 8). During the same scenario (increasing pressure Scenario), the mass input to the steam PRZ is higher than in other PRZs. The gas PRZ also has the lowest value. In general, the pressure in the loop increases with increasing temperature. The upper region of each PRZ has a different content. Figure 9 shows that the pressure in all three PRZs has increased. The pressure changes in the gas PRZ are more than other PRZs. This is due to the presence of NCG inside the gas PRZ (upper region of gas PRZ). This figure shows that the gas PRZ is more sensitive to turbulence than other PRZs. After the gas PRZ, Due to the presence of certain amounts of NCG in the mixture with Steam in upper region of PRZ, Gas-Steam PRZ is more sensitive to turbulence.

It should be noted that the design of the PRZ depends on several factors including the primary loop's inventory and reactor power. In steam PRZ, the volume of the steam is a very critical design parameter that affects the peak pressure. Also, using NCG in the PRZ design (Steam-gas PRZ and Gas PRZ) can be associated with advantages and challenges. Usually, the use of the NCG increases the peak pressure due to the lack of NCG condensation during transient conditions. Thus, in the small volume ratio of steam inside the PRZ, it seems that adding gas is not appropriate. Because it increases the peak pressure further and the pressure increases rapidly even during the small transients. Of course, from another perspective, the work of the spray is reduced by adding NCG. Also, the pure gas PRZ has the highest peak pressure but has easy control logic (Fig. 10). In other words, the use of gas PRZ makes it possible to change the pressure quickly. The gas PRZ is

the best choice for high-pressure test facilities. Also, the gas PRZ can be used passively. A summarized comparison between the types of PRZ is shown in Fig. 10. Figure 11 compares the peak pressure in the three PRZs, quantitatively. During the in-surge scenario, in the gas PRZ, the pressure is increased by approximately 2 bar during the scenario and reaches a pressure of 152 bar.

In this study, Gas-Steam PRZ has been selected and different molar fractions have been implemented. The change of pressure in the Steam-Gas PRZ is apparently different when the mole fraction of Argon varies. The peak pressure increases with the increase in Argon mole fraction. This is due to the condensation heat transfer in the presence of NCG, which decreases the heat-transfer coefficient with an increasing mole fraction of NCG. Figure 12 shows the impact of NCG in more detail. During the operation of the PRZ in the loop, the use of the NCG increases the peak pressure due to the lack of NCG condensation during transient conditions. With increasing molar fraction of NCG in the mixed region (from 37% to 57%), the peak pressure increased. The reason for reducing the peak pressure is to reduce the amount of NCG in the steam-gas mixture.

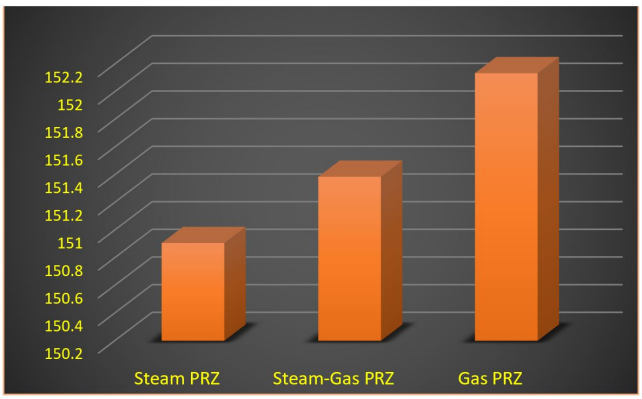


**Figure 11:** The PRZs comparison is based on their peak pressure in transients.

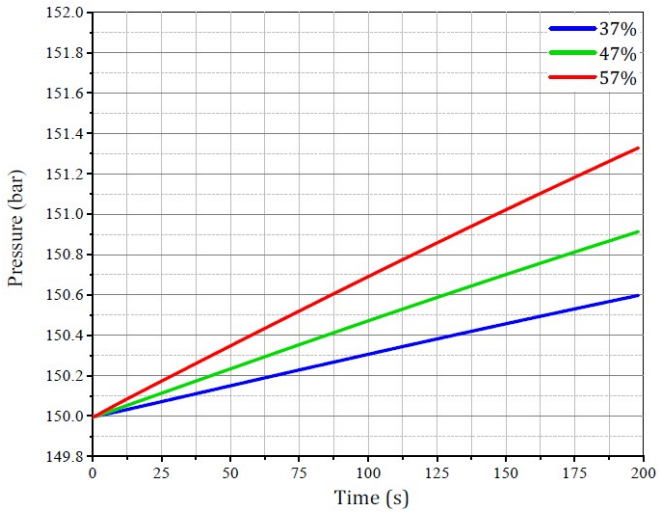


**Figure 12:** Different NCG Mole Fractions inside Steam-Gas PRZ.

## 5 Conclusions

The pressure control system (pressurizer) plays a key role in pressurized water processes. PRZs in the nuclear industry are classified into three groups. Steam PRZ is the most common type of PRZ in the nuclear industry. The Gas-Steam PRZ is another type of PRZ that is used in nuclear industries, especially in small modular reactors. The main difference between a Steam and Gas-Steam PRZ is that the upper region of a Gas-Steam PRZ is a mixture of NCG and steam. Gas PRZ is another type of PRZ, which is used NCG in the upper region of PRZ to control the pressure. in this study, three PRZ was connected to the WHPCHF loop to evaluate their performance during in-surge scenario. The pressure changes in the gas PRZ are more than other PRZs. This study shows that the gas PRZ was more sensitive to turbulence than in other PRZs. After the gas PRZ, the steam PRZ was more sensitive to turbulence. The use of gas PRZ makes it possible to change the pressure quickly due to the high peak pressure. The gas PRZ is the best choice for small reactors and high-pressure test facilities because of its controllability. Also, the gas PRZ can be used passively.

## Conflict of Interest

The authors declare no potential conflict of interest regarding the publication of this work.

## Open Access



## References

Abdallah, A. M., Mariy, A. H., Rabie, M. A., et al. (1982). Pressurizer transients dynamic model. *Nuclear Engineering and Design*, 73(3):447–453.

Baggoura, B. and Martin, W. R. (1983). Transient analysis of the three Mile island unit 2 pressurizer system. *Nuclear Technology*, 62(2):159–171.

Baghban, G., Shayesteh, M., Bahonar, M., et al. (2016). Simulating and evaluating the pressurizer dynamic behavior in various sizes. *Progress in Nuclear Energy*, 93:406–417.

Baron, R. (1973). Digital model simulation of a nuclear pressurizer. *Nuclear Science and Engineering*, 52(3):283–291.

Beak, S. (1986). A non-equilibrium three region model for transient analysis of pressurized water reactor pressurizer system. *Nucl. Technol.*, 74:213–221.

Cheng, Y.-H., Wang, J.-R., Lin, H.-T., et al. (2009). Benchmark calculations of pressurizer model for maanshan nuclear power plant using TRACE code. *Nuclear Engineering and Design*, 239(11):2343–2348.

Corradini, M. and Wu, Q. (2015). Critical Heat Flux Phenomena at HighPressure & Low Mass Fluxes: NEUP Final Report Part I: Experiments. Technical report, Battelle Energy Alliance, LLC, Idaho Falls, ID (United States).

Farman, N. F., Mahdi, S. A., and Redha, Z. A. A. (2017). Mathematical analysis of the transient dynamic of surge-in or/and surge-out of the pressurizer of PWR. *International Journal of Simulation–Systems, Science & Technology*, 18(4).

Hassan, Y. and Banerjee, S. (1996). Implementation of a noncondensable model in RELAP5/MOD3. *Nuclear Engineering and Design*, 162(2-3):281–300.

Hosseini, S. A., Shirani, A. S., Lotfi, M., et al. (2020). Design and application of supervisory control based on neural network pid controllers for pressurizer system. *Progress in Nuclear Energy*, 130:103570.

Kim, J.-W., Lee, Y.-G., and Park, G.-C. (2008). Numerical Analysis on Transient of Steam-gas Pressurizer.

Kim, T.-W., Kim, J.-W., and Park, G.-C. (2006). Development of nonequilibrium pressurizer model with noncondensable gas. *Nuclear Engineering and Design*, 236(4):375–384.

Lee, Y.-G. and Park, G.-C. (2013). TAPINS: a thermal-hydraulic system code for transient analysis of a fully-passive integral PWR. *Nuclear Engineering and Technology*, 45(4):439–458.

Lotfi, M., Menhaj, M. B., Hosseini, S. A., et al. (2020). A design of switching supervisory control based on fuzzy-PID controllers for VVER-1000 pressurizer system with RELAP5 and MATLAB coupling. *Annals of Nuclear Energy*, 147:107625.

Moghanaki, S. K. and Rahgoshay, M. (2014). Simulation of two-region and four-region models for typical PWR pressurizer and benchmark obtained results using available results. *Annals of Nuclear Energy*, 63:302–308.

O'Brien, J. E., Yoon, S.-J., Sabharwall, P., et al. (2017). High-Pressure, High-Temperature Thermal Hydraulic Test Facility for Nuclear-Renewable Hybrid Energy System Studies; Facility Design Description and Status Report. Technical report, Idaho National Lab.(INL), Idaho Falls, ID (United States).

Pini, A., Cammi, A., Colombo, L., et al. (2018). A non-equilibrium control oriented model for the pressurizer dynamics. *Progress in Nuclear Energy*, 106:102–119.

Redfield, J., Prescop, V., and Margolis, S. (1968). Pressurizer performance during loss-of-load tests at shippingport: analysis and test. *Nuclear Applications*, 4(3):173–181.

Shoghi, A., Hosseini, S. A., Shirani, A. S., et al. (2021). Development and verification of the mathematical modeling for gas-pressurizer system. *Annals of Nuclear Energy*, 164:108630.

Wang, P., He, J., Wei, X., et al. (2019). Mathematical modeling of a pressurizer in a pressurized water reactor for control design. *Applied Mathematical Modelling*, 65:187–206.

Wu, L., Jia, H., and Liu, Y. (2013). Numerical Study of the Gas-Steam Transient Behavior in the Integrated Pressurizer. In *International Conference on Nuclear Engineering*, volume 55799, page V002T03A030. American Society of Mechanical Engineers.

Wu, Y., Su, G., Qiu, S., et al. (2010). Development of a thermal-hydraulic analysis software for the Chinese advanced pressurized water reactor. *Nuclear Engineering and Design*, 240(1):112–122.

Xi, M., Wu, Y., Tian, W., et al. (2015). The influence of ocean conditions on thermal-hydraulic characteristics of a passive residual heat removal system. *Progress in Nuclear Energy*, 85:573–587.

Yoder Jr, G. L., Aaron, A., Cunningham, B., et al. (2014). An experimental test facility to support development of the fluoride-salt-cooled high-temperature reactor. *Annals of Nuclear Energy*, 64:511–517.

Zhong, X., Zhang, X., Yu, J., et al. (2019). Development of an improved non-equilibrium multi-region model for pressurized water reactor pressurizer. *Annals of Nuclear Energy*, 126:133–141.

RPE | Radiation Physics & Engineering
An International Peer-Reviewed Journal
Published by K.N. Toosi University of Technology
http://rpe.kntu.ac.ir
Research Article

Radiation Physics and Engineering 2022; 3(4):31–34
https://doi.org/10.22034/rpe.2022.342624.1089

# Kinetic investigation of tellurium hexafluoride production using the volumetric method

Amir Charkhi, Parisa Zaheri*, Amjad Sazgar, Iman Dehghan

*Nuclear Fuel Cycle Research School, Nuclear Science and Technology Research Institute, P.O. Box: 11365-8486, Tehran, Iran*

## HIGHLIGHTS

- The kinetic reaction of tellurium hexafluoride synthesis was studied using the volumetric method.
- A laboratory system was designed and constructed for the volumetric method.
- The fluorination of tellurium oxide was a first-order reaction in the temperature of $204 \pm 1$ °C.

## ABSTRACT

Since the production of tellurium hexafluoride gas requires the design of a suitable reactor system, so the study of tellurium oxide fluorination kinetics is of great importance. For this purpose, a novel laboratory system was designed and constructed to study the fluorination reactions by the volumetric method. Fluorine gas was injected into the reactor containing a tellurium oxide pellet, and the reaction was studied by following the changes in pressure of the gas phase using a pressure transmitter instrument. In this volumetric system, the kinetic parameters of the reaction between tellurium oxide pellet and fluorine gas have been derived for a pressure range of 137.9 and 181.2 kPa by monitoring the gas phase pressure. The reaction temperature was adjusted to $204 \pm 1$ °C using a heater. The results showed that the fluorination reaction of tellurium oxide is a first-order reaction. The reaction rate constant is calculated to be $6.86 \times 10^{-4}$ $s^{-1}$.

## KEYWORDS

Volumetric method
Flourination
Tellurium hexaflouride
Kinetic parameters

## HISTORY

Received: 18 May 2022
Revised: 21 June 2022
Accepted: 5 July 2022
Published: Autumn 2022

## 1 Introduction

Due to the use of stable tellurium isotopes, enrichment of these isotopes has been considered as one of the goals of the Atomic Energy Organization. For example, different tellurium isotopes are used to produce iodine radionuclides, which are used in the treatment of hyperthyroidism, thyroid cancers, treatment and diagnostic kits for adrenal cancers, and so on (Williams Jr, 1948). The primary method of enrichment of these isotopes is the gas centrifuge method, in which tellurium hexafluoride gas is injected into the centrifuge and separated (Benedict et al., 1981). Since the production of this gas requires the design of a suitable reactor system, so the study of tellurium fluorination reaction kinetics is of great importance.

To measure the reaction rate in solid-gas systems, the solid is usually formed into a pellet and contacted with the gas stream under controlled temperature and pressure. The product of the reaction may be gaseous (such as the production of tellurium hexafluoride) or solid (such as the desulfurization of sulfides) (Szekely, 2012).

The reports of gas-solid reactions indicate that most studies have focused on reactions that produce solid products (such as metal oxidation processes). Instead, few studies have been done on the processes that lead to a gaseous product, such as the fluorination reaction of tellurium, molybdenum, and so on (Labaton and Johnson, 1959).

The methods that can be used to examine the progress of the solid-gas reactions are classified into two groups:

1. Measurement of changes in solid,

2. Measurement of changes in the gas phase.

The techniques used in the first group include continuous measurement of solid weight (gravimetric method). In the second group, it is possible to measure the changes in gas pressure to study the reaction kinetic (volumetric method) (Szekely, 2012).

The basis of the volumetric method is the expansion of the gas between the reference volume and the reactor chamber, which includes a solid sample. First, the gas

*Corresponding author: pzaheri@aeoi.org.ir

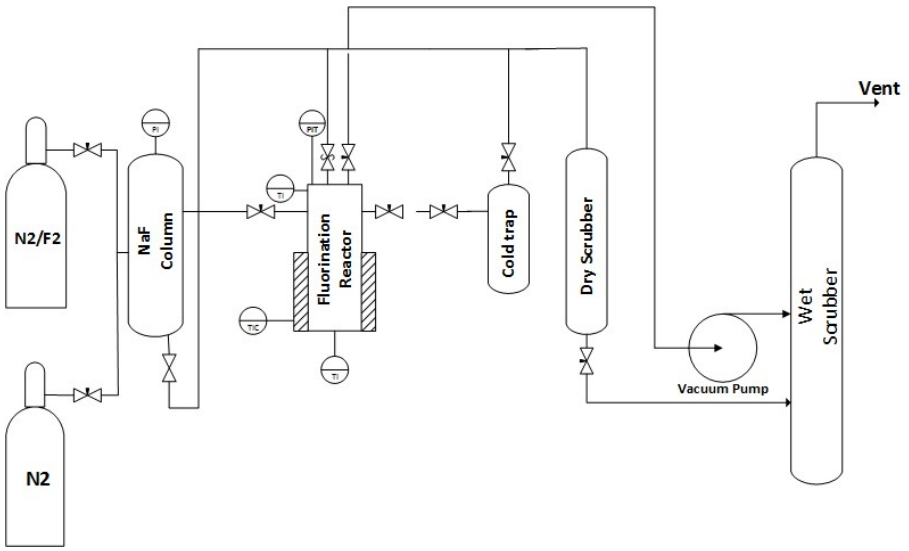


**Figure 1:** The shematic of the laboratory system.

pressure is adjusted to the reference volume, and then the valve is opened. After a certain pressure is reached in the reactor chamber, the valve closes, and the reaction begins. Pressure changes in the reactor are recorded over time. In this method, the type of valve used and the pressure transmitter must be selected correctly. Also, to increase the accuracy of the volumetric method, the system leakage rate should be carefully checked and reach zero. Temperature control is also important, and the system must reach thermal equilibrium before the reaction can begin. The attractive feature of the volumetric method is its robustness and relatively low cost (Wang et al., 2021).

In this research work, a laboratory system was designed and built. In this system, the kinetic parameters of the tellurium hexafluoride production were derived by the volumetric method.

Tellurium hexafluoride can be prepared by the reaction between tellurium oxide and fluorine at 150 to 300 °C as follow (Campbell and Robinson, 1956):

$$TeO_2 + 3F_2/N_2 \longrightarrow TeF_6 + O_2 + N_2 \qquad (1)$$

Before this study was made, no fundamental data on the kinetics of this reaction were available.

## 2 Experimental

### 2.1 Materials

Tellurium oxide ($TeO_2$) and sodium fluoride (NaF) powder were purchased from Sigma Aldrich (Table 1). The mixture of fluorine and nitrogen gas capsule (40% fluorine) was provided by Soreh company in Iran.

**Table 1:** The properties of $TeO_2$ and NaF.

| Properties | Molar mass ($g.mol^{-1}$) | Appearance | Density ($g.cm^{-3}$) |
|---|---|---|---|
| $TeO_2$ | 159.60 | white solid | 5.670 |
| NaF | 41.98 | white solid | 2.558 |

### 2.2 Apparatus and methods

A laboratory system was designed and used for kinetic studying (Fig. 1). Based on the fluorine gas reactivity, allowable temperature, and pressure limits, all apparatus, valves, and instruments in this system were made of stainless steel 316 (Barbe et al., 2007). After cleaning the system, leak tests were carried out to ensure that the system had stable pressure. Then, passivation was done in stages by increasing concentrations and pressure of fluorine, allowing the metal fluoride film to develop on the metal surface and thus preventing any further fluorine reaction. The system was vacuumed, then a mixture of nitrogen and fluorine gas (40% fluorine) was passed through a column packed with NaF granules to remove HF of the gas. After that, the gas is injected into the reactor (containing $TeO_2$ pellet with a specific weight) until a certain pressure. The reactor was heated by a furnace with adjustable temperature. The reaction was followed by observing changes in the pressure of the reactor, and these changes were recorded by a pressure recorder at different times. At the end of the reaction, the gas was directed into a dry scrubber (containing activated alumina) and then a wet scrubber (containing NaOH solution) to remove all gases. A cold trap was used to collect the product.

## 3 Results and discussion

### 3.1 Calibration

To determine the leakage rate of the system, fluorine gas was injected into the reactor without reactant ($TeO_2$ pellet) under reaction conditions. The leakage rate was calculated by recording changes in reactor pressure over time. According to the presented results in Fig. 2, the leakage rate of fluorine gas from the reactor is approximately 0.6 $Pa.s^{-1}$, which was considered in calculating the reaction kinetics.

### 3.2 Measuring the volume of the reactor

Since the volumetric method is used to study the reaction kinetics, it is essential to determine the exact volume of the reactor. This volume includes the volume of the reactor, the volume of the terminal, the volume of dead spaces between the valves, pressure gauge, and terminal connections. For this purpose, nitrogen gas pressure changes were measured after injection into the vacuumed reactor several times. Using the ideal gas law, the volume of the reactor was calculated to be 145.3 ml.

### 3.3 Kinetics of the reaction

The experiments were done at four initial pressure of 181.2, 158.9, 153.9, and 137.9 kPa. The temperature of the reactor was adjusted to $204 \pm 1$ °C in all experiments. The pressure changes recorded over a period of 25 minutes are shown in Fig. 3. As expected from Eq. (1), the pressure in the system decreases with the reaction between fluorine and tellurium oxide. To determine the kinetics of the reaction, $TeF_6$ production rate was considered as follows:

$$\frac{1}{S}\frac{\mathrm{d}n_{\mathrm{TeF_6}}}{\mathrm{d}t} = K\,C_{F_2}^{a} \tag{2}$$

where $S$ is the surface area of the $TeO_2$ pellet, and $n_{\mathrm{TeF_6}}$ is the mole of $TeF_6$ gas. $K$ and $CF_2$ are the rate constant and fluorine gas concentration, respectively.

According to Eq. (1), the system pressure changes are written as Eq. (3):

$$\frac{\mathrm{d}P_T}{\mathrm{d}t} = K'(3P_T - 2.6\,P_0)^{a} \tag{3}$$

$$\ln(-\frac{\mathrm{d}P_T}{\mathrm{d}t}) = \ln(K') + a \times \ln(3P_T - 2.6\,P_0) \tag{4}$$

where $P_0$ and $P_T$ are the pressure at $t = 0$ and $t = t$, respectively.

Using the experimental data, $\ln(-\mathrm{d}P_T/\mathrm{d}t)$ was drawn in terms of $\ln(3\,P_T - 2.6\,P_0)$. The results in Fig. 4 show that the fluorination reaction of tellurium is a first-order reaction. The rate constant determined for this reaction was $6.86 \times 10^{-4}$ $s^{-1}$.

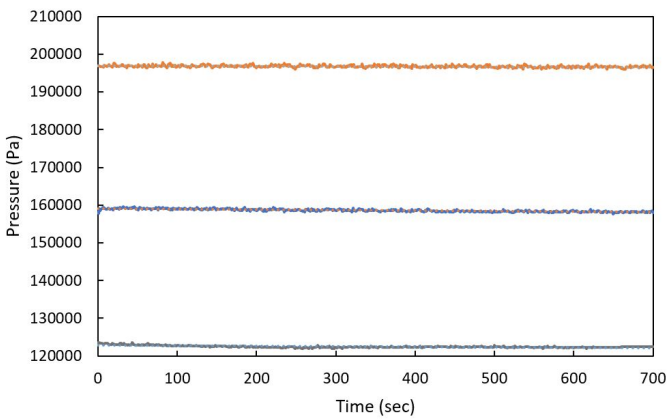


**Figure 2:** The results of leakage rate of the system.

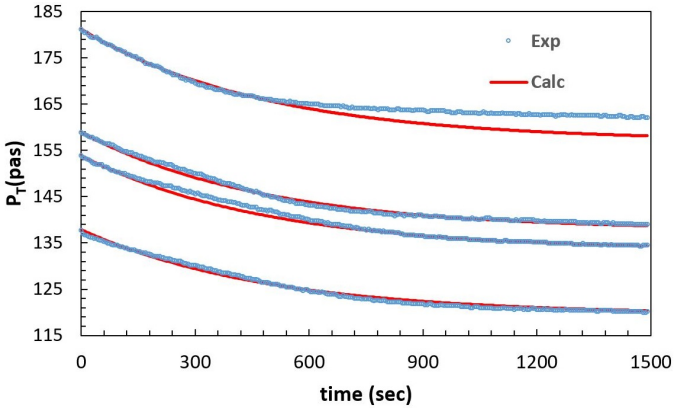


**Figure 3:** The experimental and calculated pressure changes with time.

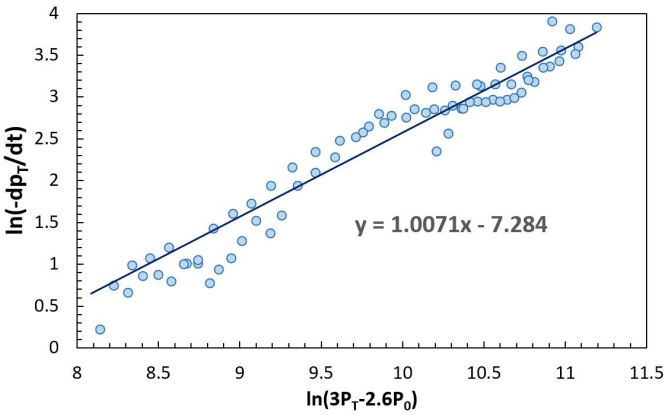


**Figure 4:** $\ln(-\mathrm{d}P_T/\mathrm{d}t)$ vs. $\ln(3P_T - 2.6P_0)$.

To examine the accuracy of the obtained results, $P_T$ was calculated and compared with experimental data using the Average Absolute Relative Error (AARE) equation:

$$AARE(\%) = \frac{\sum_{i=1}^{n} \frac{|P_T^{\mathrm{Exp.}} - P_T^{\mathrm{Calc.}}|}{P_T^{\mathrm{Exp.}}}}{n} \times 100 \tag{5}$$

in which $n$ is the number of experimental points.

The AARE (%) value was calculated to be 0.56%. This shows a good agreement between experimental and calculated values, and the kinetic model can predict the reaction kinetics of tellurium oxide with fluorine gas at $204 \pm 1$ °C.

## 4 Conclusions

In this study, a laboratory system was designed and constructed to study the fluorination reactions by the volumetric method. This system was used to derive the kinetic parameters of the tellurium hexafluoride production for a pressure range of 137.9 and 181.2 kPa and reaction temperature of $204 \pm 1$ °C. Monitoring the gas phase pressure showed that the reaction rate depends on the pressure at a constant temperature. A linear relationship was shown

to exist between the reaction rate and pressure of fluorine. The rate constant determined for this reaction was $6.86 \times 10^{-4}$ $s^{-1}$.

## Conflict of Interest

The authors declare no potential conflict of interest regarding the publication of this work.

## Open Access



## References

Barbe, J., Barbier, J.-P., Currie, J., et al. (2007). Code of practice-compressed fluorine and mixtures with inert gases.

Benedict, M., Pigford, T. H., and Levi, H. W. (1981). *Nuclear chemical engineering*. McGraw-Hill Education.

Campbell, R. and Robinson, P. (1956). 668. The fluorination of tellurium. Ditellurium decafluoride and tellurium oxyfluorides. *Journal of the Chemical Society (Resumed)*, pages 3454–3458.

Labaton, V. and Johnson, K. (1959). The fluorides of uranium-III kinetic studies of the fluorination of uranium tetrafluoride by flourine. *Journal of Inorganic and Nuclear Chemistry*, 10(1-2):74–85.

Szekely, J. (2012). *Gas-solid reactions*. Elsevier.

Wang, J.-Y., Mangano, E., Brandani, S., et al. (2021). A review of common practices in gravimetric and volumetric adsorption kinetic experiments. *Adsorption*, 27(3):295–318.

Williams Jr, R. R. (1948). Nuclear Chemistry of Tellurium: Chemical Effects of Isomeric Transition. *The Journal of Chemical Physics*, 16(5):513–519.

RPE | Radiation Physics & Engineering
An International Peer-Reviewed Journal
Published by K.N. Toosi University of Technology
http://rpe.kntu.ac.ir
Research Article

Radiation Physics and Engineering 2022; 3(4):35–41
https://doi.org/10.22034/rpe.2022.341568.1088

# Comparison of conversion factor methods in spectrometric dosimetry systems based on NaI(Tl) scintillation detectors

Akbar Abdi Saray[a], Hossein Zaki Dizaji[b,*], Seyed Mortaza Taheri Balanoji[a]

[a] *Physics Department, Faculty of Science, Urmia University, Urmia, Iran*
[b] *Faculty of Science, Imam Hossein Comprehensive University, Tehran, Iran*

## HIGHLIGHTS

- Dosimetry methods have been developed based on the analysis of detector output data.
- Three different techniques are studied to obtain the conversion coefficients.
- The subdivision of measured spectrum method is provided to modify and improve the evaluated conversion coefficients.
- The dose quantity calculation error percentage reduces by utilizing the improved coefficients.

## ABSTRACT

To monitor personal safety in the fields of biomedical and health physics, it is necessary to be aware of radiation doses to protect the health and safety of persons. Radiation protection quantities such as air kerma, ambient dose equivalent, and exposure dose rate are obtained by the measured spectrum to determine energy-dependent conversion coefficients/factors. This study aims to obtain and compare an ambient dose equivalent to $H^*(10)$ from the measured gamma-ray spectra by the NaI(Tl) scintillation detector using two various methods. The first method, which is based on the detector response function to find the conversion function, is called the $G(E)$ method. The second method is subdividing the measured gamma-ray spectra into the multiple energy bins, and then obtaining the ambient dose equivalent by using conversion coefficient functions ($\omega(E)$), which were determined by the conversion coefficients ($\omega_i$) of each energy bin for three energy intervals of $\leq$ 185 keV, 185 to 850 keV, and $\geq$ 850 keV. To calculate the detector response matrix and the conversion coefficients of each region of energy, the Monte Carlo simulation code was used for the quasi-mono energetic gamma radiation sources and the synthetic spectra. The results indicate that using the technique based on subdividing the measured spectrum into multiple energy bins helps to avoid the inverse detector response matrix dimension limitations that occur in the $G(E)$ method and also have a lower error percentage in the dose quantity calculation. Consequently, NaI(Tl) scintillation detector has an excellent potential to replace the classical dose rate instruments, i.e. Geiger-Muller, for the early warning of environmental radiation monitoring.

## KEYWORDS

Detection
Monte Carlo simulation
Ambient dose
Spectro-Dosimeter method
Energy-dependent coefficients

## HISTORY

Received: 9 May 2022
Revised: 28 June 2022
Accepted: 5 July 2022
Published: Autumn 2022

## 1 Introduction

In radiation protection and health physics, to evaluate and minimize the risk of radiation-induced effects on radiation workers, it is increasingly important to know the dose value in a real-time manner. Awareness of dose values is necessary for imaging procedures for diagnosis, treatment, and disease prevention. These procedures, particularly in Iran, are generally conducted with the use of radioactive materials, such as the planar (gamma camera) and single-photon emission computed tomography (SPECT). The thermoluminescence dosimeter (TLD) and photographic dosimeter, known as integrating dosimeter (Attix, 2008a), can not directly represent the real-time dose values, and they are not convenient for emergency scenarios. On the other hand, pulse-mode dosimeters such as the Geiger-Muller tube, silicon p-i-n photodiode (Si-PIN), silicon photomultiplier (SiPM), and scintillation detectors such as cerium chloride doped with lanthanum bromide ($LaBr_3$(Ce)), thallium doped with cesium iodide (CsI(Tl)), thallium doped with sodium iodide (NaI(Tl)), and high-purity germanium (HPGe) can

*Corresponding author: kpzaki@ihu.ac.ir

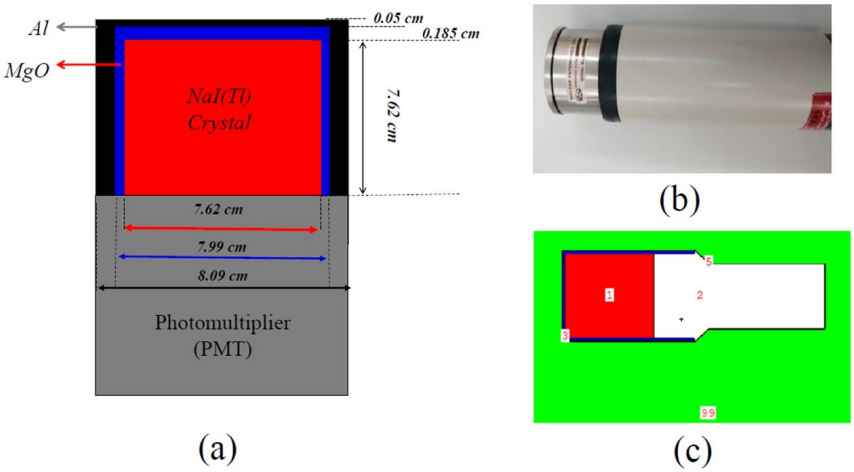


**Figure 1:** The schematic of an NaI scintillator: a) A 2D representation, b) experimental, and c) MCNPX model.

be used in the real-time measuring of the air kerma rate or the ambient dose equivalent rate $H^*(10)$ (Wang et al., 2015). The major advantage of the above-mentioned nuclear radiation detectors is that they measure the energy of charged particles and gamma-rays, in addition to dose quantity. It means that nuclear radiation detectors as spectra-dosimeter instruments can easily be used for the qualitative and quantitative analysis of radioisotopes. However, there are some risks associated with these procedures. Improving these measurement instruments with the best equipment or new software approaches can facilitate the better measurement of the radiation field and dosage simultaneously (Moriuchi and Miyanaga, 1966; Casanovas et al., 2016; Dizaji et al., 2014).

Since scintillation detectors have higher average atomic numbers than the tissue, it is impossible to determine the dose values directly from the detector output. Hence, the photon energy response of scintillation detectors must be modified. For this purpose, there exist various methods, e.g., coupling p-i-n diode or silicon photomultiplier to CsI(Tl) scintillation detector (Buzhan et al., 2018; Park et al., 2020), using software methods such as unfolding (Rahman and Cho, 2010), and deconvolution (stripping method) methods (Camp and Vargas, 2014).

Portable detectors such as NaI(Tl) scintillator can be used as a spectrometric system to measure the gamma-ray energy spectra. The energy spectrum measured with this detector provides information on photon energy for any gamma radiation sources; however, this energy spectrum includes partial energy deposition events due to the Compton scattering and gamma-ray escape. Therefore, by correcting and modifying the output of the NaI(Tl) scintillation detector, the measurement of the essential dosimeter quantities such as air kerma or ambient dose equivalent $H^*(10)$ is possible.

In the present work, the methodology for calculating air kerma and the ambient dose equivalent from the measured pulse-height distribution using the NaI(Tl) scintillation detector based on two software methods is described and compared. The first method, which is frequently called the $G(E)$ method, is based on the detector response function to find the conversion function. The second method is based on subdividing the measured gamma-ray spectra into multiple-energy bins to identify the conversion coefficients ($\omega_i$) for each energy bin. We intend to obtain $H^*(10)$ from the measured gamma-ray spectra by the NaI(Tl) scintillator using the two above-mentioned methods. As a result, we see that the subdivision of the measured spectrum into multiple energy bins to avoid the dimension limitations of the inverse detector response matrix, which occurred in the $G(E)$ method, is more favorable. The calculated error percentage in the subdivision method is much less than that in the $G(E)$ method.

## 2 Simulation and Method

### 2.1 *Monte Carlo (MC) simulation*

MC simulation is the most accurate technique for tracking particle transport in any material. Due to the limited availability of quasi-mono-energetic gamma-ray sources to construct a spectrum database, it is necessary to precisely simulate the detector and its responses to the radiation sources. The MCNP4C code uses the track structure MC simulation, which provides valuable information for understanding the initial pattern of energy depositions in materials, detector response function, and pulse-height spectrum (Briesmeister, 2000). The gamma spectrum of the scintillation detector is the combination of partial (Compton scattering) and full energy deposition (photoelectric effect and escape peaks) events.

In the present work, the MCNP4C code is used to obtain the pulse-height spectra of the NaI(Tl) detector when it is exposed to gamma-ray sources. The detector model used in the simulation is the same as the scintillation detector used in a laboratory for experimental studies, which is a cylindrical NaI(Tl) ($7.62 \times 7.62$ cm$^2$) as a sensitive volume covered by a MgO and Al layer. The inner structure and the density of this detector material are shown in Fig. 1 and Table 1, respectively.

According to energy calibration and resolution calibration, the Full Width at Half Maximum (FWHM) func-

**Table 1:** The material compositions and geometry of the NaI(Tl) detector.

| Component | Density (g.cm$^{-3}$) | Size (cm) |
|---|---|---|
| NaI(Tl) (Crystal) | 3.67 | $7.62 \times 7.62$ |
| Al (Layer) | 2.70 | 0.05 |
| MgO (Layer) | 3.58 | 0.185 |
| Photomultiplier tube (PMT) (to be treated as a vacuum aluminum cylinder) | 2.70 | $8.32 \times 23$ |

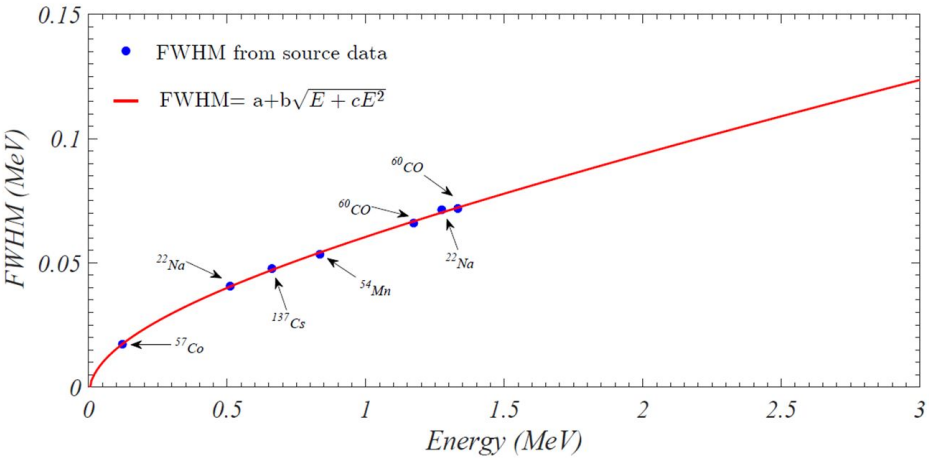


**Figure 2:** FWHM variation curve as a nonlinear function of energy.

tion is considered to recover the statistical factors for broadening the photopeak with the energy axis or applying the Gaussian Energy Bordering (GEB) with a Gaussian function. The photopeaks in the measured spectra are Gaussian shaped and are not sharp as in the simulations. Therefore, in MC simulations, the GEB is used to broaden the photopeaks. The measured peaks are often represented by FWHM, where the best fitting function of FWHM can be written as (Salgado et al., 2012):

$$FWHM = a + b\sqrt{E + cE^2} \tag{1}$$

where a, b, and c are the fitting parameters. For this work, the values of these parameters for the NaI(Tl) detector are $a = -0.0033$ MeV, $b = 0.0584$ MeV$^{1/2}$, and $c = 0.1911$ MeV$^{-1}$. With these coefficients, the FWHM variation curve is a nonlinear function of energy. By considering the energy and resolution calibration of the NaI(Tl) detector, the simulation approach can be compared with the experimental results. Figure 2 shows a graph of the FWHM function for an NaI(Tl) scintillation detector.

In gamma-ray spectroscopy, the relation between the measured spectrum $N$ and the fluence of the incident gamma-rays $\overrightarrow{\phi}$ can be expressed as:

$$\overrightarrow{N} = R.\overrightarrow{\phi} \tag{2}$$

where $R$ is the detector response matrix or the library of the detector responses to monoenergetic gamma-rays. The response matrix $R$ was calculated by using the F8 tally of the MCNP4C code. Setting the number of primary particles at $10^8$ keeps the uncertainties well below 0.2% for parallel-beam mono-energetic gamma-rays with energies ranging from 0.03 to 3 MeV.

### *2.2 The $G(E)$ function method*

#### 2.2.1 The $G(E)$ function by using the response matrix

In the spectro-dosimetry method, the dosimetric quantities, e.g., ambient dose equivalent, air kerma, or exposure dose, can be calculated from the pulse-height spectrum of any spectrometric detectors. By knowing the ambient dose equivalent response function (fluence to ambient dose equivalent conversion factors), which was introduced and defined by the ICRP 47 document (ICRP, 1996), dose quantities can be calculated. Furthermore, the ambient dose equivalent for each given fluence energy can be described as:

$$H^*(10)(E) = \overrightarrow{C}(E).\overrightarrow{\phi}(E) \tag{3}$$

where $\overrightarrow{C}(E)$ is the fluence to ambient dose equivalent conversion factor. By substituting Eq (2) into Eq (3), the ambient dose equivalent can be presented as:

$$H^*(10) = \overrightarrow{C}.(R^{-1}.\overrightarrow{N}) = (\overrightarrow{C}.R^{-1}).\overrightarrow{N} \tag{4}$$

Correspondingly, the dose conversion factor $G(E)$ can be determined as:

$$G(E) = \overrightarrow{C}.R^{-1} \tag{5}$$

It should be noted that the $G(E)$ function is dependent on both the detector geometry and the direction of incident irradiation. Moreover, the low energy resolution of the NaI(Tl) detector affects the calculation of the inverse detector response matrix. Due to the zero determination of the square response matrix in the inverse calculation of the matrix, the dimensions of the response matrix were

reduced from 1024 × 1024 to 50 × 50. The detector response matrix was assumed to be a 50 × 50 square matrix with involved energies ranging from 0.03 to 3 MeV with energy intervals of 60 keV. To reduce the dose value errors, it is recommended to use a polynomial function that has the power of the natural logarithm of the energy with a gradient-descent method, least-square method, and adaptive moment estimation method (Park et al., 2020).

### 2.2.2 The $G(E)$ function by using the least-square estimation

In general, the relation between the measured spectrum $N(E)$ and the fluence of the incident gamma spectrum $\phi(E_0)$ can be expressed as (Tsoulfanidis and Landsberger, 2021):

$$N(E) = \int_{E_{min}}^{E_{max}} R(E, E_0)\, \phi(E_0)\, \mathrm{d}E_0 \tag{6}$$

where $R(E, E_0)$ is the response function, which represents the gamma rays of energy $E_0$ that is the deposited energy in the NaI(Tl) scintillation detector. By using the ambient dose equivalent $H^*(10)(E_0)$ generated at a given fluence rate $\phi(E_0)$ from Eq. (3), the fluence-to-ambient dose equivalent conversion factors for specific gamma-ray energy can be described as (Attix, 2008b):

$$\begin{aligned} C(E_0) &= \frac{H^*(10)(E_0)}{\phi(E_0)} \\ &= \int_{E_{min}}^{E_{max}} R(E, E_0)\, G(E)\, \mathrm{d}E \end{aligned} \tag{7}$$

Here, $G(E)$ is a spectrum to dose conversion function. The $G(E)$ function can be expressed as a polynomial function with the power of the natural logarithm of the energy approximated (Huang, 2018; Tsuda and Saito, 2017):

$$G(E) = \sum_{K=1}^{KMAX} A(K) \times \left(\log_{10}(E)\right)^{K-M-1} \tag{8}$$

where $KMAX$ is the maximum term number of the polynomial equation, $M$ is a constant, and $A(K)$ refers to the coefficient for the $K^{th}$ term in the $G(E)$ equation, which was calculated by applying the least-square method. Consequently, the ambient dose equivalent can be written as:

$$H^*(10) = \sum_{i=1}^{k} N(E_i)\, G(E_i) \tag{9}$$

in which $k$ is the number of channels in spectrometric systems. Figure 3 shows the $G(E)$ function curve in Eq. (5) and Eq. (8) for $KMAX = 8$.

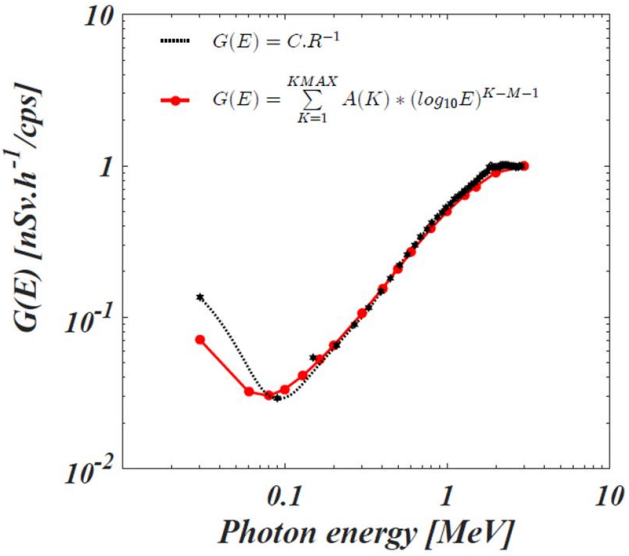


**Figure 3:** The conversion factors ($G(E)$ function) for the response spectrum of a NaI(Tl) scintillation detector.

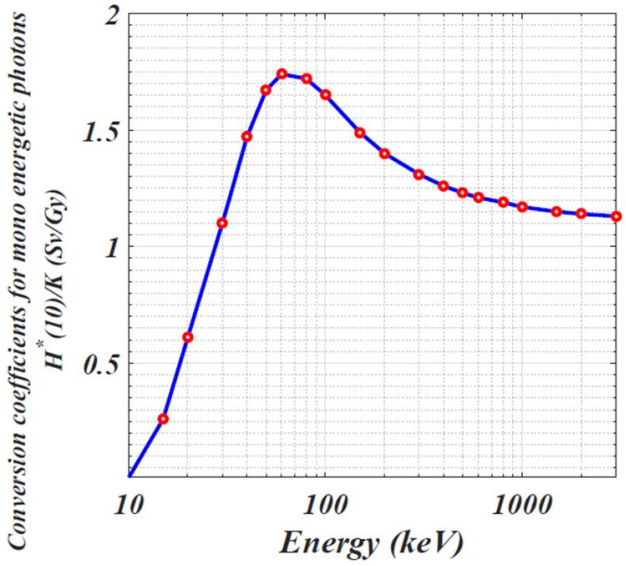


**Figure 4:** The conversion coefficients (ICRP, 1996) for monoenergetic photons relating air kerma to ambient dose equivalent.

### *2.3 The subdivision of the measured gamma-ray spectrum method*

The second method is subdividing the measured gamma-ray spectra into multiple energy bins to obtain the energy-dependent conversion coefficient, instead of using the $G(E)$ function method. In this method, the total energy deposited in the NaI(Tl) detector is well correlated with the air kerma values, which are measured by ionization chambers. There is a relationship between the number of counts in the measured spectra and the air kerma responsible for these counts (Lowder et al., 1964) due to the ratio of mass energy-absorption coefficients between air and crystal in the energy range of 0.4 to 3 MeV which is relatively constant. Therefore, the total energy deposited in the

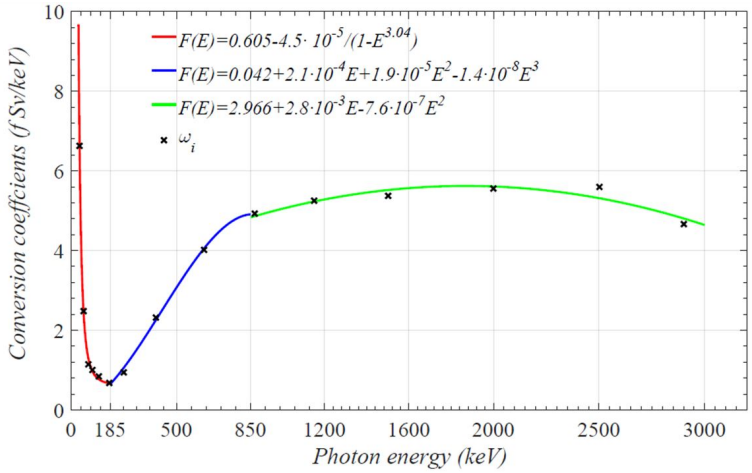


**Figure 5:** The energy-dependent conversion coefficient functions ($\omega(E)$) for a NaI(Tl) scintillation detector.

NaI(Tl) detector may be proportionate to air kerma with a unique conversion coefficient. However, at low gamma-ray energies, due to the photoelectric effect, the ratio of mass energy absorption is not constant (Grasty et al., 1992). As a result, we can not use a unique conversion coefficient between the deposited energy in the detector and kerma in the air. To solve this problem, the spectrum is divided into several energy regions $\nu$, and for each one, a calibrated conversion coefficient is applied. The total air kerma resulting from the sum of $\nu$ particle values of kerma can be calculated from each energy region. The relationship between the air kerma and energy deposited in the detector for each region can be written as:

$$K = \sum_{i=1}^{\nu} \omega_i \, n_i \, E_i \tag{10}$$

where $\omega_i$ is the energy-dependent conversion coefficient of the energy region $i$, and the value $n_i E_i$ corresponds to the energy deposited in the region $i$. the conversion coefficients that should be used to convert air kerma to ambient dose equivalent $H^*(10)$ have been given in the ICRP 47 document (ICRP, 1996). Also, these conversion coefficients $H^*(10)/K$ for monoenergetic photons are displayed in Fig. 4.

If the energy-dependent conversion coefficient $\omega_i$ is obtained by the MC simulation, the deposited energy in the detector can be directly related to the ambient dose equivalent, $H^*(10)$. Then, Eq. (10) is changed to:

$$H^*(10) = \sum_{i=1}^{\nu} \omega_i \, n_i \, E_i \tag{11}$$

To solve Eq. (11), which is a system of linear equations, the Cholesky decomposition method is used (Madar, 2015). Thereby, the general solution obtained is:

$$\omega_i = \frac{H^*(10)_i - \sum_{j=1}^{i-1} n_{ij} \, E_j \, \omega_j}{n_{ii} \, E_i} \tag{12}$$

The selected position of these desired energy boundaries in Eq. (12), including most of the energy in the photopeak deposited in the associated window selected energy regions in the MC simulation together with the obtained conversion coefficients, are summarized in Table 2. It should be mentioned that in each energy region, there must be at least one strong energy line, and the number of conversion coefficients is equal to the number of sources used. Clearly, the number of these conversion factors for measuring the ambient dose value is less than the conversion factors in the $G(E)$ method.

Figure 5 shows three different fitting functions defined in the energy ranges $\leq$ 185 keV, 185 to 850 keV, and $\geq$ 850 keV to be used for generating the values of the energy-dependent conversion coefficients $\omega_i$ for the NaI(Tl) detector. By using these fitting functions, Eq. (11) can be replaced by:

$$H^*(10) = \sum_{i=1}^{\nu} \omega_i(E_i) \, n_i \, E_i \tag{13}$$

**Table 2:** Conversion coefficients $\omega_i$ calculated for the NaI(Tl) detector.

| $\gamma$ peaks (keV) | Energy regions (keV) | Conversion coefficient (pSv.keV$^{-1}$) |
|---|---|---|
| 40 | 25 - 55 | $6.63 \times 10^{-3}$ |
| 60 | 55 - 65 | $2.47 \times 10^{-3}$ |
| 80 | 65 - 95 | $1.14 \times 10^{-3}$ |
| 100 | 95 - 105 | $1.01 \times 10^{-3}$ |
| 130 | 105 - 155 | $8.39 \times 10^{-4}$ |
| 180 | 155 - 205 | $6.76 \times 10^{-4}$ |
| 250 | 205 - 295 | $9.48 \times 10^{-4}$ |
| 400 | 295 - 505 | $2.32 \times 10^{-3}$ |
| 630 | 505 - 755 | $4.03 \times 10^{-3}$ |
| 870 | 755 - 985 | $4.92 \times 10^{-3}$ |
| 1150 | 985 - 1315 | $5.26 \times 10^{-3}$ |
| 1500 | 1315 - 1685 | $5.37 \times 10^{-3}$ |
| 2000 | 1685 - 2315 | $5.55 \times 10^{-3}$ |
| 2500 | 2315 - 2685 | $5.59 \times 10^{-3}$ |
| 2900 | 2685 - 3115 | $4.66 \times 10^{-3}$ |

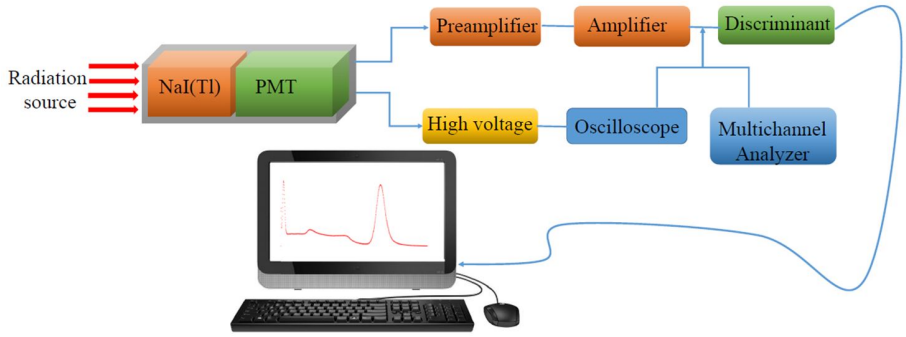


**Figure 6:** Demonstration of a scintillation detector system.

**Table 3:** Experimental and simulation dose values.

| Source | Value | $H^*(10)(\mu Sv.h^{-1})$ | $K(\mu Gy.h^{-1})$ |
|---|---|---|---|
| Cs-137 | Experimental: $\omega(E)$ | 0.309 ± 0.03 | 0.254 ± 0.02 |
| | $G(E) = \overrightarrow{C}.R^{-1}$ | 0.288 ± 0.05 | 0.231 ± 0.08 |
| | $G(E) = \sum_{K=1}^{KMAX} A(K) \times \left(\log_{10}(E)\right)^{K-M-1}$ | 0.297 ± 0.04 | 0.249 ± 0.05 |
| | Theoretical | 0.314 | 0.262 |
| Co-60 | Experimental: $\omega(E)$ | 0.208 ± 0.01 | 0.168 ± 0.02 |
| | $G(E) = \overrightarrow{C}.R^{-1}$ | 0.172 ± 0.06 | 0.147 ± 0.04 |
| | $G(E) = \sum_{K=1}^{KMAX} A(K) \times \left(\log_{10}(E)\right)^{K-M-1}$ | 0.189 ± 0.03 | 0.159 ± 0.06 |
| | Theoretical | 0.201 | 0.172 |

## 3 Results and discussion

To investigate the structure of this method in the dosimetry field, gamma radiation sources are placed at a distance of 10 cm from the detector surface, and the NaI(Tl) detector output signal is fed into a preamplifier. Then its output is connected to an amplifier, which is used to avoid shifting the baseline. The output signal of the amplifier is directly given to the multi-channel analyzer to obtain the energy spectrum of each gamma-ray source. The NaI(Tl) scintillation detector readouts for various gamma-ray sources are experimentally obtained using the geometry shown in Fig. 6. The main point for using the conversion coefficients to obtain the air kerma or ambient dose equivalent in the experimental process should subtract the background spectrum (the environmental spectrum without any gamma-ray sources) from the measured spectrum.

Table 3 summarizes the results of the measured and calculated air kerma rate and ambient dose equivalent rate of some standard gamma-radiation sources, which have been obtained in this work.

The results show that due to the low energy resolution of the NaI(Tl) detector (energy resolution of 7.1% at the energy peak of 662 keV) and also the limitation in taking an inverse of the detector response matrix, the probability of finding the conversion factor for measuring the error of air kerma and ambient dose equivalent can be reduced by using the subdivision technique. Uncertainty values, which are shown in Table 3, are less than 10%, which is acceptable for general guidance on uncertainty levels based on the ICRP recommendations (ICRU, 2016). To this end, by using the subdividing gamma-ray spectrum method, we can decrease the uncertainty of measuring the dose value with the NaI(Tl) detector in the dosimetry field.

## 4 Conclusions

In this study, we show that in addition to detecting radioisotope radiations emitted from natural radioactive sources by the NaI(Tl) detector, the dose rate values of the spectra can be calculated by determining the conversion factors. Two diverse methods including the $G(E)$ function and the subdivision of the energy spectra have been studied and compared. The results show that the subdivision method is more beneficial compared to the $G(E)$ function method since it uses a smaller number of conversion coefficients and avoids the limitation of the detector response function. Furthermore, the error percentage of measuring the dose rate using the subdivision method is less than that of using the $G(E)$ function method. For this purpose, the conventional dosimeter, e.g. the Geiger-Muller tube, can be replaced with these real-time spectrometric systems for emergency scenarios.

## Conflict of Interest

The authors declare no potential conflict of interest regarding the publication of this work.

## Open Access



## References

Attix, F. H. (2008a). *Introduction to radiological physics and radiation dosimetry*. John Wiley & Sons.

Attix, F. H. (2008b). *Introduction to radiological physics and radiation dosimetry*. John Wiley & Sons.

Briesmeister, J. F. (2000). MCNP-A General Monte Carlo N-Particle Transport Code, Version 4C. *LA-13709-M*.

Buzhan, P., Karakash, A., and Teverovskiy, Y. (2018). Silicon Photomultiplier and CsI (Tl) scintillator in application to portable H*(10) dosimeter. *Nuclear Instruments and Methods in Physics Research Section A: Accelerators, Spectrometers, Detectors and Associated Equipment*, 912:245–247.

Camp, A. and Vargas, A. (2014). Ambient dose estimation H*(10) from LaBr3 (Ce) spectra. *Radiation Protection Dosimetry*, 160(4):264–268.

Casanovas, R., Prieto, E., and Salvadó, M. (2016). Calculation of the ambient dose equivalent H*(10) from gamma-ray spectra obtained with scintillation detectors. *Applied Radiation and Isotopes*, 118:154–159.

Dizaji, H. Z., Kakavand, T., and Davani, F. A. (2014). Spectrometry and dosimetry of fast neutrons using pin diode detectors. *Nuclear Instruments and Methods in Physics Research Section A: Accelerators, Spectrometers, Detectors and Associated Equipment*, 741:84–87.

Grasty, R., Multala, J., and Lemmela, H. (1992). Monitoring man-made radiation using a 256 channel portable gamma-ray spectrometer. In *8. International congress of the International Radiation Protection Association (IRPA8)*.

Huang, P. (2018). Measurement of air kerma rate and ambient dose equivalent rate using the G(E) function with hemispherical CdZnTe detector. *Nuclear Science and Techniques*, 29(3):1–7.

ICRP (1996). *ICRP Publication 74: Conversion coefficients for use in radiological protection against external radiation. International Commission on Radiological Protection*, volume 23. Elsevier Health Sciences.

ICRU (2016). *ICRU report 39, International Commission on Radiological Units*, volume 21. International Commission on Radioation Units and Measurements.

Lowder, W., Beck, H., and Condon, W. (1964). Spectrometric determination of dose rate from natural and fall-out gamma radiation in the United States, 1962–1963. *Nature*, 10.

Madar, V. (2015). Direct formulation to Cholesky decomposition of a general nonsingular correlation matrix. *Statistics & probability letters*, 103:142–147.

Moriuchi, S. and Miyanaga, I. (1966). A spectrometric method for measurement of low-level gamma exposure dose. *Health Physics*, 12(4):541–551.

Park, K., Kim, J., Lim, K. T., et al. (2020). Improvement of a spectrum-to-dose conversion function for electronic personal dosimeters. *Journal of Instrumentation*, 15(02):C02018.

Rahman, M. and Cho, G. (2010). Unfolding low-energy gamma-ray spectrum obtained with NaI(Tl) in air using matrix inversion method. *Journal of Scientific Research*, 2(2):221–226.

Salgado, C. M., Brandão, L. E. B., Schirru, R., et al. (2012). Validation of a NaI(Tl) detector's model developed with MCNP-X code. *Progress in Nuclear Energy*, 59:19–25.

Tsoulfanidis, N. and Landsberger, S. (2021). *Measurement & detection of radiation*. CRC press.

Tsuda, S. and Saito, K. (2017). Spectrum–dose conversion operator of NaI(Tl) and CsI(Tl) scintillation detectors for air dose rate measurement in contaminated environments. *Journal of Environmental Radioactivity*, 166:419–426.

Wang, Y., Zhou, R., and Yang, C. (2015). Verification of the method of average angular response for dose measurement on different detectors. *Journal of Instrumentation*, 10(07):T07001.